3. GLOBAL OCEANS

a. Overview—R. Lumpkin

The global oceans impact weather events and are the memory of the climate system at time scales from subseasonal to millennial. They absorb vast amounts of heat, carbon dioxide, and other properties from the atmosphere, store them throughout the water column, transport them via a network of interconnected surface and subsurface currents, and ultimately return them to the atmosphere or sequester them in sediments.

Focusing on 2018, this chapter describes the evolution of sea surface temperature (SST), ocean heat content, salinity, air–sea fluxes, sea level, surface currents, phytoplankton, and ocean inorganic carbon. As we are reminded in section 3i, the ocean is responding to an atmosphere with higher carbon dioxide levels than at any time in the last 800 000 years. Globally-averaged sea level reached a record high in 2018—for the seventh consecutive year (section 3f). Globally-averaged SST cooled slightly since the record El Niño year of 2016 but is still far above the climatological mean (section 3b). Meanwhile, the deeper ocean continues to warm year after year (section 3c). In the Atlantic Ocean, SST and heat content anomaly patterns show the characteristic cold-warm-cold tripole fingerprint expected of a slowing meridional overturning circulation (MOC; Caesar et al. 2018). Cooling in the subpolar North Atlantic was driven by turbulent heat fluxes from increased winds (section 3e). Climatologically, this cooling is balanced by northward advection of warm water in the MOC, but this advection has decreased (Smeed et al. 2018) as the MOC responds to a warmer high-latitude atmosphere and an increase in surface buoyancy due to ice melt (Sevellac et al. 2017). As anticipated in a warming climate, the hydrological cycle over the ocean is accelerating (Rhein et al. 2013): dry regions are becoming drier and wet regions rainier (section 3e). These changes are reflected in sea surface salinity anomaly patterns (section 3d). Meanwhile, the upper 600 m of the western Atlantic have steadily become saltier from 2005 to 2018; 2018 is the first year with all monthly salinity anomalies in the upper 1500 m of the Atlantic saltier than the long-term mean (section 3d). In contrast, the eastern North Atlantic is becoming fresher. Year-to-year changes in rainfall and salinity are also seen, including the 2018 drought and high salinity anomalies over the Maritime Continent (sections 3d,e). Due to anomalously shallow mixed layers exposing phytoplankton to prolonged sunlight, and possibly lower nutrient input due to increased stratification, concentrations of chlorophyll-*a* were suppressed by 10%–30% in warm SST regions of the tropical Pacific, western North Pacific, and subtropical North Atlantic (section 3h).

Our understanding of the climate system has advanced, and there is more to learn about what was observed in 2018. New estimates of ocean uptake of anthropogenic CO_2 are increased by ~20% by better accounting for riverine input (section 3i). A dramatic new global map of changes in the concentration of anthropogenic CO_2 from the 1980s to the 1990s depicts the global MOC pathways sequestering this CO_2 into the abyssal and deep oceans (section 3i; Gruber et al. 2019). The GRACE Follow-On satellite mission began data collection in May 2018 and will help determine how much of the sea level rise in 2017–18 was due to ice melt (versus thermal expansion; section 3f).

Unfortunately, this *State of the Climate* report was not able to include a section on changes in the Atlantic Meridional Overturning Circulation (AMOC). However, significant recent progress in understanding variations of the AMOC has been made. During 2004–17, the AMOC at 26°N shifted to a reduced state in approximately 2008 (Smeed et al. 2018). The first results from the Overturning in the Subpolar North Atlantic Program (OSNAP) demonstrate that Labrador Sea Water formation changes may not significantly impact overall year-to-year AMOC variability (Lozier et al. 2019). In fact, at interannual time scales, AMOC variability in the South Atlantic at 34.5°S has significant variations in both the eastern and western boundaries, in contrast to the primarily western boundary-associated variability at 26°N (Meinen et al. 2018), highlighting the role of the South Atlantic in modifying water masses carried by the AMOC. Furthermore, new AMOC observing arrays are now in place at both 11°S and 47°N and are expected to produce results soon (Hummels et al. 2015; Roessler et al. 2015; Frajka-Williams et al. 2019). As such, an invigorated AMOC section should be available in the 2019 report.

Finally, chapter sidebars highlight the *Sargassum* inundations that have plagued Caribbean beaches since 2011 (Sidebar 3.1) and the destructive red tide blooms off the Florida coasts in 2017–19 (Sidebar 3.2), both of which have caused enormous economic damage. The year 2018 set a new record for areal coverage of tropical Atlantic *Sargassum*, raising the question, "Does this reflect a climate-change driven regime shift in the ecology of these macroalgae?" The red tide caused significant decreases in fishery yields and tourism revenues in 2018, demonstrating the urgent need to better understand the relevant mechanisms, predict future blooms, and provide mitigation strategies.

b. Sea surface temperatures—B. Huang, J. Kennedy, Y. Xue, and H.-M. Zhang

Global SST in 2018 is assessed using the Extended Reconstruction Sea-Surface Temperature version 5 (ERSSTv5; Huang et al. 2017); Daily Optimum Interpolation SST (DOISST; Reynolds et al. 2007); and U.K. Met Office Hadley Centre SST version 3 (HadSST.3.1.1.0; Kennedy et al. 2011a, 2011b). ERSSTv5 is a monthly 2° × 2° SST product from 1854 to present based on in situ observations only. The DOISST is a daily 0.25° × 0.25° SST product for the modern satellite era from September 1981 to present using both in situ and satellite observations. The HadSST.3.1.1.0 is a monthly 5° × 5° SST product from 1850 to present using in situ observations only. SST anomalies (SSTAs) are calculated relative to their own climatologies over 1981–2000.

Averaged over the global oceans, ERSSTv5 analysis shows that SSTAs continued to decrease from the record El Niño year maximum of 0.44° ± 0.05°C in 2016 to 0.38° ± 0.05°C in 2017 and 0.33° ± 0.05°C in 2018. Uncertainty ranges indicate the 95% confidence level estimated from a 1000-member ensemble based on ERSSTv4 (Huang et al. 2016). Later in this section, ERSSTv5 results are compared to those from DOISST and HadSST3.1.1.0.

Figure 3.1a shows annually averaged SSTA in 2018. In the Pacific Ocean, SSTA was +0.5°C to +1.0°C in the northwestern North Pacific and near the Bering Strait, about +0.5°C in the eastern North Pacific extending from the U.S.–Mexico coasts toward the western tropical Pacific, and about +0.5°C in the midlatitude South Pacific between 30°S and 60°S. SSTA was about −0.5°C in the southeastern tropical Pacific between 150°W and 70°W. In the Atlantic, SSTA was +0.5°C to +1.5°C in the western North Atlantic between 25°N and 45°N, +1.0° to +1.5°C in the northern North Atlantic stretching towards the Arctic, and about +0.5°C in the midlatitude South Atlantic near 45°S. SSTA was about −0.5°C south of Greenland near 50°N and west of Africa near 15°N. In the Indian Ocean, SSTA was small.

In comparison with SST in 2017, SST in 2018 was −0.2°C to −0.5°C cooler over most of the global oceans (Fig. 3.1b). However, SST increased by 0.5°–1.0°C in the northern North Pacific, by about 0.2°C in the central equatorial Pacific and the South Pacific between 20°S and 60°S, and by about 0.5°C in the western North Atlantic near 40°N and the South Atlantic between 30°S and 60°S.

The cooling of −0.2°C to −0.5°C in the southeastern tropical Pacific in 2018 (Fig. 3.1b) was associated with the weak La Niña of 2017–18. Tropical Pacific

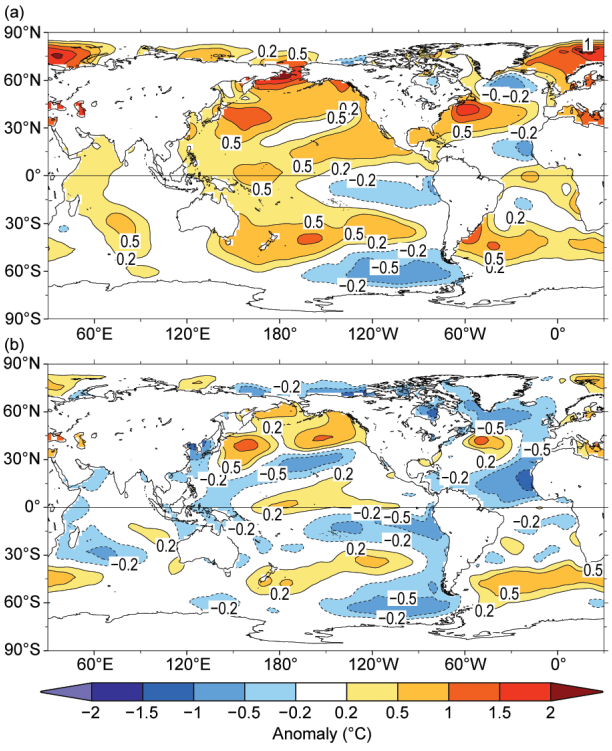

Fig. 3.1. (a) Annually averaged SSTA of ERSSTv5 in 2018, and (b) Difference of annually averaged SSTAs between 2018 and 2017. SSTAs (°C) are relative to 1981–2010 climatology.

SSTAs in December–January–February (DJF) and March–April–May (MAM) of 2018 (Figs. 3.2a,b) were −0.5°C to −1.0°C, about 1 standard deviation (σ) colder than the average of 1981–2010. The warming of 0.2°C in the western-central tropical Pacific in 2018 (Fig. 3.1b) resulted from the emerging El Niño of 2018–19 (see section 4b). Western-central tropical Pacific SSTAs in June–July–August (JJA) and September–October–November (SON) of 2018 (Figs. 3.2c,d) were +0.5°C to +1.0°C, which were 1σ to 2σ warmer than average.

Warming in the northern North Pacific (Fig. 3.1b) was associated with a higher SSTA that developed throughout 2018 and intensified with time, and was 1σ to 2σ warmer than average (Fig. 3.2). The higher SSTA resulted in a weak negative Pacific Decadal Oscillation (PDO; Mantua and Hare 2002) index throughout 2018. In the South Pacific (Fig. 3.2), an SSTA of +0.5°C to +1.0°C (1σ –2σ warmer than average) was sustained southeast of Australia along 45°S throughout 2018, while an SSTA of –1.0°C (1σ colder than average) was sustained near 60°S between 60°W and 170°W.

In the North Atlantic, SSTAs in 2018 were +1°C to +1.5°C (2σ warmer than average) in the western

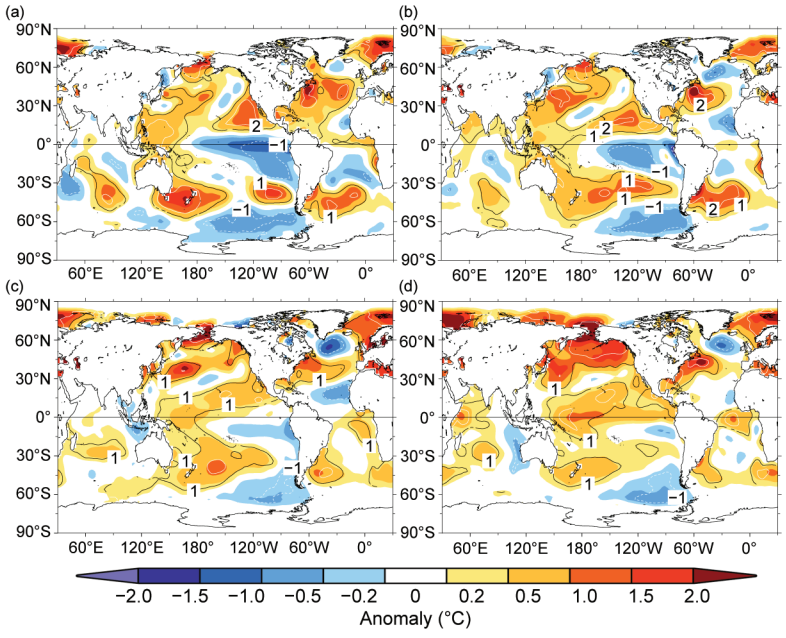

Fig. 3.2. Seasonal averaged SSTAs of ERSSTv5 (°C; shading) for (a) Dec 2017 to Feb 2018, (b) Mar to May 2018, (c) Jun to Aug 2018, and (d) Sep to Nov 2018. The normalized seasonal mean SSTA based on the seasonal mean standard deviation over 1981–2010 are indicated by contours of −1 (dashed white), 1 (solid black), and 2 (solid white).

basin between 25°N and 45°N and in the Nordic Seas (Fig. 3.2). In contrast, SSTAs in 2018 were −0.5°C to −1.0°C (1σ colder than average) south of Greenland in MAM, JJA, and SON (Figs. 3.2b,c,d). This SSTA pattern of warm-cold-warm has been sustained since 2014, which may be associated with variations of the Atlantic Meridional Overturning Circulation (AMOC; Sevellec et al. 2017; Caesar et al. 2018). In the midlatitude South Atlantic along about 45°S, SSTAs in 2018 were +1.5°C in DJF (Fig. 3.2a), decreased to +1.0°C in MAM (Fig. 3.2b) and +0.5°C in JJA (Fig. 3.2c) and SON (Fig. 3.2d). These SSTAs were about 1σ to 2σ above average. In the tropical Atlantic, SSTAs in 2018 were about +0.5°C (1σ –2σ) in DJF (Fig. 3.2a), disappeared in MAM (Fig. 3.2b), and reemerged in JJA and SON (Figs. 3.2c,d).

In the tropical Indian Ocean, SSTAs in 2018 were weak in DJF, MAM, and JJA (Figs. 3.2a,b,c). A pattern similar to the Indian Ocean Dipole (IOD; Saji et al. 1999) can be identified in SON (Fig. 3.2d). In the southern Indian Ocean between 20°S and 60°S, SSTAs in 2018 were about −0.5°C (1σ colder than average) near 30°E and +1.0°C near 75°E in DJF (Fig. 3.2a), and about +0.5°C (1σ warmer than average) between 60°E and 90°E in MAM, JJA, and SON (Figs. 3.2b,c,d).

Overall, warming trends of SSTs since the 1950s or 1880s over the global oceans can be identified (Figs. 3.3a,b), although the global average SST has cooled since 2016. The linear trends of globally annually averaged SSTs were 0.10° ± 0.01°C decade^{-1} over 1950–2018 (Table 3.1). The warming appears largest in the tropical Indian Ocean (Fig. 3.3g) and smallest in the North Pacific (Fig. 3.3d). The uncertainty of the trends represents the 95% confidence level of the linear fitting.

In addition to the long-term SST trend, interannual variations of SSTAs can be seen in all ocean basins, although the amplitude of variations was smaller in the Southern Ocean. The variations associated with the Atlantic Multidecadal Oscillation (AMO; Wanner et al. 2001) can be identified with a warm period over the 1990s–2010s and a cold period over the 1950s–80s (Fig. 3.3f). Similarly, SSTA in the North Pacific (Fig. 3.3d) decreased from the 1950s to the later 1980s and increased from the later 1980s to the 2010s.

SSTAs in ERSSTv5 were compared with those in DOISST and HadSST3.1.1.0. All data sets were averaged to monthly 2° × 2° grid for a comparison purpose. Comparisons (Fig. 3.3) indicate that the SSTA departures of DOISST and HadSST.3.1.1.0 from ERSSTv5 are largely within 2σ (gray shading in Fig. 3.3). The 2σ envelope was derived from a 1000-member ensemble analysis based on ERSSTv4 (Huang et al. 2016), and ±2σ and −2σ uncertainties are shaded above and below the SSTAs of ERSSTv5. However, SSTAs were slightly higher in the 1950s–70s and the 1920s–30s in HadSST.3.1.1.0 than in ERSSTv5. Similarly, SSTAs were slightly higher in the 2000s–2010s in HadSST.3.1.1.0 and DOISST than in ERSSTv5, particularly in the Southern Ocean. Previous studies (Huang et al. 2015; Kent et al. 2017) showed that these SSTA differences were mostly attributed to the differences in bias corrections to ship observations in those products. These SST differences resulted in a slightly weaker SSTA trend in HadSST.3.1.1.0 over both 1950–2018 and 2000–18 (Table 3.1). In contrast, SST trends were slightly higher in DOISST over 2000–18.

Table 3.1. Linear trends (°C decade^{-1}) of annually and regionally averaged SSTAs from ERSSTv5, HadSST3, and DOISST. The uncertainties at 95% confidence level are estimated by accounting for AR(1) effect on the degrees of freedom of annually averaged SST series.

Product	Region	2000–2018	1950–2018
HadSST.3.1.1.0	Global	0.131 ± 0.069	0.084 ± 0.016
DOISST	Global	0.162 ± 0.062	N/A
ERSSTv5	Global	0.164 ± 0.085	0.100 ± 0.013
ERSSTv5	Tropical Pacific (30°S–30°N)	0.182 ± 0.201	0.100 ± 0.028
ERSSTv5	North Pacific (30°–60°N)	0.297 ± 0.141	0.068 ± 0.038
ERSSTv5	Tropical Indian Ocean (30°S–30°N)	0.197 ± 0.110	0.140 ± 0.019
ERSSTv5	North Atlantic (30°–60°N)	0.118 ± 0.107	0.105 ± 0.049
ERSSTv5	Tropical Atlantic (30°S–30°N)	0.127 ± 0.110	0.108 ± 0.021
ERSSTv5	Southern Ocean (30°–60°S)	0.127 ± 0.068	0.099 ± 0.016

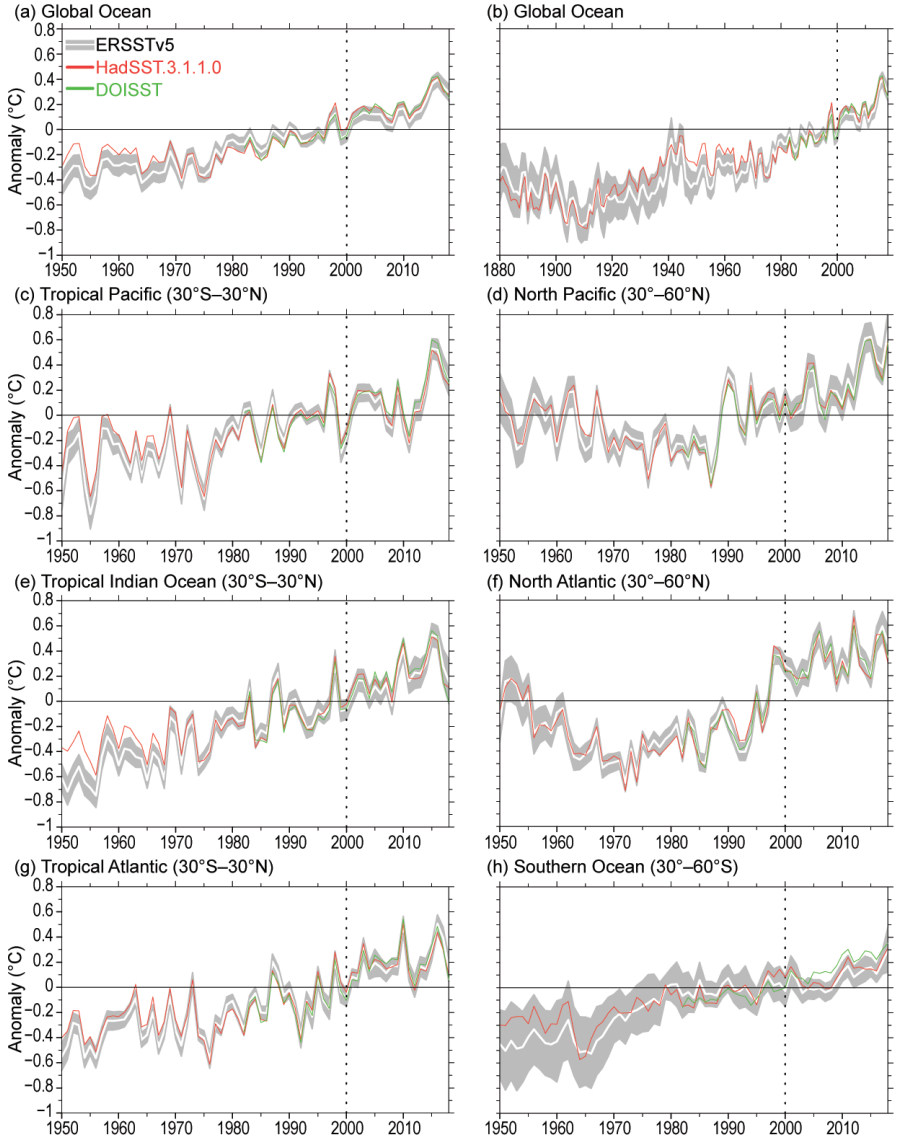

Fig. 3.3. Annually averaged SSTAs of ERSSTv5 (solid white) and 2σ (gray shading) of ERSSTv4, SSTAs of DOISST (solid green), and SSTAs of HadSST.3.1.1.0 (solid red) in 1950–2018 except for (b). (a) Global, (b) Global in 1880–2018, (c) Tropical Pacific, (d) Tropical Indian Ocean, (e) Tropical Atlantic, (f) North Pacific, (g) North Atlantic, and (h) Southern Ocean. The year 2000 is indicated by a vertical black dotted line.

SIDEBAR 3.1: UNPRECEDENTED SARGASSUM BLOOMS IN THE TROPICAL ATLANTIC—C. HU AND M. WANG

Starting in 2011, large amounts of pelagic *Sargassum* washed onto the beaches of many Caribbean islands almost every summer (Gower et al. 2013; Wang and Hu 2017). While these brown macroalgae, comprised primarily of *S. natans* and *S. fluitans*, provide important habitat to many marine animals such as fish, shrimp, crabs, and turtles (Rooker et al. 2006; Witherington et al. 2012; Lapointe et al. 2014; Doyle and Franks 2015) and thus can influence various trophic levels and the ocean's biogeochemistry (Parr 1939; Culliney 1970; Carpenter and Cox 1974; Phlips and Zeman 1990; Lapointe 1995; Turner and Rooker 2006; Zepp et al. 2008), excessive *Sargassum* on beaches represents a nuisance and a health hazard as well as a burden to local management, tourism, and economy. Numerous local and international news media have reported how local governmental agencies and environmental groups in the Caribbean reacted to the increased *Sargassum* beaching events (Franks et al. 2011; Higgins 2011; Kirkpatrick 2015; Schell et al. 2015; Stasi 2015). In 2015, Mexico called its Navy to take action (Partlow and Martinez 2015). In 2018, Barbados declared a national emergency due to excessive *Sargassum* inundation (Rawlins-Bentham 2018).

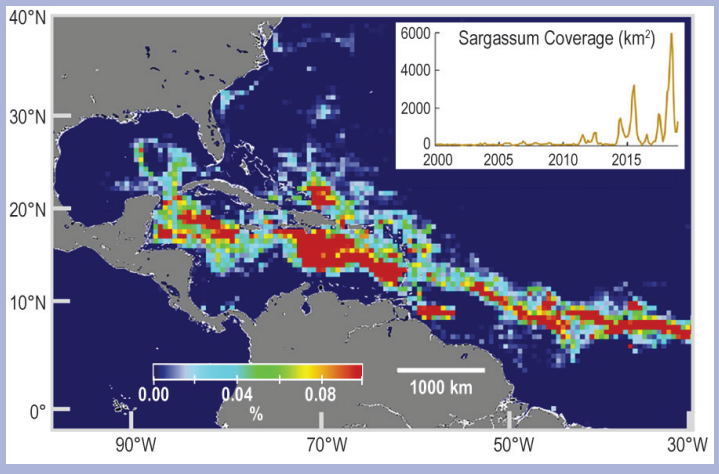

FIG. SB3.1. *Sargassum* areal density in Aug 2018 derived from MODIS observations (Wang and Hu 2016; Wang 2018). The inset shows the total *Sargassum* areal coverage (if they are aggregated together) between 2000 and 2018. The coverage extended further east to at least 10°W (not shown here).

Given these unprecedented *Sargassum* amounts found in the Caribbean after 2011, many questions remain unanswered. For example, what caused the recent blooms? Where do they originate? Are we entering a regime shift where recurring blooms become a new norm as a result of climate change?

Satellite images show that the Caribbean *Sargassum* originated from the central Atlantic (Gower et al. 2013; Wang and Hu 2016, 2017). A region off the Amazon River mouth was speculated to be the source region (Gower et al. 2013), while more recent studies indicate the entire central Atlantic, extending from west Africa to the Lesser Antilles islands, could provide initial seeds (Franks et al. 2016; Wang 2018). Figure SB3.1 shows the *Sargassum* density distributions in the Tropical Atlantic including the central Atlantic, Caribbean Sea, and Gulf of Mexico. Unpublished data even show the eastward extension of the coverage to at least 10°W. In this example, the *Sargassum* is estimated to cover an area of >4,000 km^2 if aggregated together. Using a conversion factor determined from field measurements (Wang et al. 2018), the total *Sargassum* wet biomass is estimated to be at least 12 million metric tons. Assuming a 50:1 biomass:Chl*a* ratio for the water-column phytoplankton, in *Sargassum*-occupied waters, *Sargassum* biomass is comparable to water-column phytoplankton, while the carbon content of *Sargassum* may also represent a significant portion of total particulate organic carbon (Wang et al., 2018). Clearly, the unprecedented *Sargassum* amount in the Tropical Atlantic may significantly affect the ocean's ecology and biogeochemistry.

Satellite images show the seasonality and long-term trend in the amount of *Sargassum* found in the Caribbean Sea (Fig. SB3.1, inset). The amount usually peaks in summer and reaches minimum in winter, a possible consequence of favorable growth conditions (water temperature, nutrient and light availability) during spring. While Gower et al. (2013) only showed the initial bloom year of 2011, the new time-series shows an unambiguous increasing trend, with annual fluctuations, in subsequent years, with 2018 being the historical record year (Langin 2018).

Several hypotheses have been proposed on why a sudden increase occurred in 2011 and what caused the annual fluctuations after 2011. Rising SST, enhanced nutrient inputs from major rivers, dust depositions, and equatorial upwelling, as well as recent climate changes and ocean current variations may have created favorable conditions for the unprecedented *Sargassum* blooms in the Tropical Atlantic (Franks et al. 2011; Franks et al. 2014; Johnson et al. 2013; Djakouré et al. 2017). Indeed, under a changing climate where coastal eutrophication and other environmental conditions may lead to increased macroalgae blooms (Smetacek and Zingone 2013), the recurrent *Sargassum* blooms in the Tropical Atlantic may represent a regime shift. Currently, the scientific community is facing challenges on understanding exactly the reasons behind bloom initiation, maintenance, dissipation, and their ecological and biogeochemical implications. On the other hand, the unprec-

CONT. SIDEBAR 3.1: UNPRECEDENTED SARGASSUM BLOOMS IN THE TROPICAL ATLANTIC—C. HU AND M. WANG

edented amount of *Sargassum* experienced across much of the Caribbean may provide opportunities to develop innovative methods to fully utilize the macroalgae for fertilizers, biofuel, and other uses. In the meantime, the one-way transport from the central Atlantic to the Caribbean makes it relatively easy to provide early warning of bloom likelihood in the Caribbean (Wang and Hu 2017), and near real-time satellite imagery together with surface ocean currents can be used continuously to guide field experiment and resource management (Hu et al. 2016).

Finally, *Sargassum* blooms have also been reported in other regions in recent years. For example, in the East China Sea, an unprecedented bloom of *Sargassum horneri* occurred in spring 2017, which was speculated to be a result of a warm winter and accumulated eutrophication due to local aquaculture (Qi et al. 2017). Although *S. horneri* is a different species that usually grows on rocks, the initial bloom year of 2012 in this western Pacific region poses the question of whether it is simply a coincidence with the initial bloom year of 2011 in the Caribbean, or the global ocean has experienced subtle shifts to favor *Sargassum* growth in recent years. Clearly, more fundamental research is required to understand their response to environmental conditions under a changing climate.

c. Ocean heat content—G. C. Johnson, J. M. Lyman, T. Boyer, L. Cheng, C. M. Domingues, J. Gilson, M. Ishii, R. E. Killick, D. Monselesan, S. G. Purkey, and S. E. Wijffels

The ocean has an enormous heat capacity. One degree of warming in the global ocean stores about 1000 times the heat energy of one degree of warming in the atmosphere. Ocean warming accounts for about 93% of the total increase in Earth's energy storage from 1971 to 2010, compared to the atmosphere's 1% (Rhein et al. 2013). Ocean currents transport substantial amounts of heat (Talley 2003). Ocean heat storage and transport play large roles in ENSO (Johnson and Birnbaum 2017), tropical cyclone development (Goni et al. 2009), rates and variations in sea level rise (section 3f), and melting of ice sheet outlet glaciers around Greenland (Castro de la Guardia et al. 2015) and Antarctica (Schmidtko et al. 2014).

Maps of annual (Fig. 3.4) upper (0–700 m; or to the ocean floor where it is shallower) ocean heat content anomaly (OHCA) relative to a 1993–2018 baseline mean are generated from a combination of in situ ocean temperature data and satellite altimetry data following Willis et al. (2004) and using Argo (Riser et al. 2016) data downloaded in January 2019. Near-global average seasonal temperature anomalies (Fig. 3.5) versus pressure from Argo data (Roemmich and Gilson 2009, updated) since 2004 and in situ global estimates of OHCA (Fig. 3.6) for three pressure layers from seven different research groups (including that responsible for the 2000–6000 m estimate) are also discussed.

The 2017/18 tendency of 0–700-m OHCA (Fig. 3.4b) shows an increase in a band across much of the equatorial Pacific north of about 15°S and a decrease in a band to the north. The node between is located around 5°N in the west and 10°N in the central and east Pacific, near the North Equatorial Countercurrent, which, consistently, was anomalously strong in 2018 (see Fig. 3.18a). This pattern is strongly reminiscent of the tilting mode involved in the recharge of warm water in the equatorial Pacific prior to El Niño (Meinen and McPhaden, 2000). The tendency is toward increases in the North Pacific north of about 10°N in the west and 30°N in the east. Tendencies south of 15°S in the Pacific are patchier: east of Australia cooling is apparent, then warming southeast of New Zealand, then cooling again west of the Drake Passage. Throughout much of the Pacific, the 2018 upper OHCA is generally above the long-term average, with the most notable departures being a narrow band of below average values along ~10°N, a patchy region of low values in the central South Pacific (Fig. 3.4a), and low values west of Drake Passage.

In the Indian Ocean, the 2017/18 tendency of 0–700-m OHCA (Fig. 3.4b) is patchy, with warming in many locations, some cooling in the western Arabian Sea and in the center of the basin south of the equator, but no striking large-scale patterns. Upper OHCA values for 2018 were above the 1993–2017 mean in much of the Indian Ocean (Fig. 3.4a), with the notable exception of a persistent patch of low values in the western equatorial region that formed in 2017 and was discussed in last year's report (Johnson et al. 2018) and a prominent cool patch west of Australia.

The 2017/18 tendencies of 0–700-m OHCA (Fig. 3.4b) in the Atlantic Ocean show warming most noticeable in the western boundary current extensions of both hemispheres, although as usual those energetic, eddy-rich regions exhibited both warming and cooling tendencies. The 2017/18 cooling tendency was most prominent in a band just north of the equator, in a patch located between Madeira and the Strait of Gibraltar, and in the North Sea and Norwegian Sea. With these relatively small changes from 2017 to 2018, the 2018 anomalies (Fig. 3.4a) look

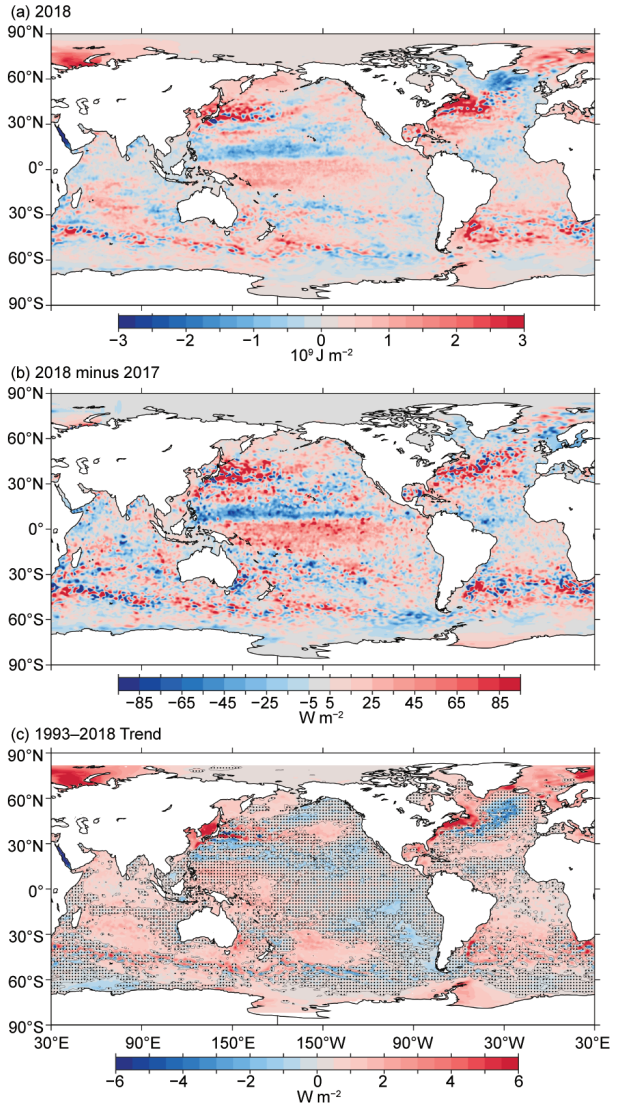

Fig. 3.4. (a) Combined satellite altimeter and in situ ocean temperature data estimate of upper (0–700 m) OHCA (×10⁹ J m⁻²) for 2018 analyzed following Willis et al. (2004), but using an Argo monthly climatology and displayed relative to the 1993–2018 baseline. (b) 2018–2017 combined estimates of OHCA expressed as a local surface heat flux equivalent (W m⁻²). For (a) and (b) comparisons, note that 95 W m⁻² applied over one year results in a 3 × 10⁹ J m⁻² change of OHCA. (c) Linear trend from 1993–2018 of the combined estimates of upper (0–700 m) annual OHCA (W m⁻²). Areas with statistically insignificant trends are stippled.

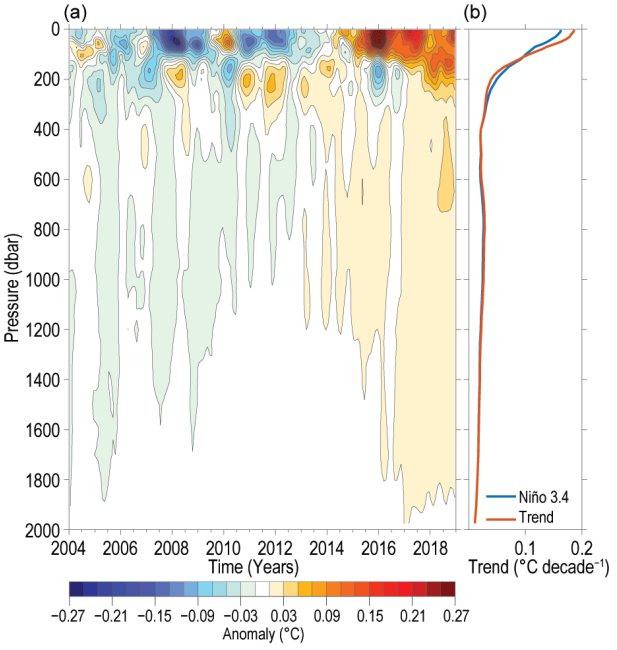

Fig. 3.5. (a) Near-global (65°S–80°N, excluding continental shelves, the Indonesian seas, the Sea of Okhostk, the Caribbean Sea, and the Gulf of Mexico) integrals of monthly ocean temperature anomalies [°C; updated from Roemmich and Gilson (2009)] relative to record-length average monthly values, smoothed with a 5-month Hanning filter and contoured at odd 0.02°C intervals (see colorbar) vs. pressure and time. (b) Linear trend of temperature anomalies over time for the length of the record in (a) plotted vs. pressure in °C decade⁻¹ (orange line), and trend with a Niño3.4 regression removed (blue line) following Johnson and Birnbaum (2017).

much like those in 2017. The large cold area south of Greenland, in the vicinity of the Irminger Sea, has persisted since at least 2014 and the warm conditions off the east coast of North America since around 2009 (see previous *State of the Climate* reports). The only other prominent areas in the Atlantic colder than the 1993–2018 average were in the Labrador Sea and just north of the equator in the western Atlantic. The latter may be associated with a change in the strength of the North Brazil Current and its retroflection (https://www.aoml.noaa.gov/phod/altimetry/cvar/nbc/transport.php).

The large-scale statistically significant (Fig. 3.4c) regional patterns in the 1993–2018 local linear trends of upper OHCA are quite similar to those from 1993–2017 (Johnson et al. 2018). The areas with statistically significant negative trends are found mostly south of Greenland in the North Atlantic, south of the Kuroshio Extension in the North Pacific, and in a small portion of the eastern South Pacific. Those areas are quite small compared with those with statistically significant positive trends, which include much of the rest of the Atlantic Ocean, the region around the Maritime Continent and the western tropical Pacific, nearly the entire Indian Ocean, most of the marginal seas except the Red Sea, and much of the South Pacific and south Indian Oceans. As noted in previous reports, the apparent warming and cooling trends adjacent to Antarctica are located in both in

situ and altimeter data-sparse regions and are not as robust as suggested by the statistics that do not reflect undersampling.

Near-global average seasonal temperature anomalies (Fig. 3.5a) reflect both a long-term warming trend (Fig. 3.5b, orange line) and ENSO redistributing heat (e.g., Roemmich and Gilson 2011) from the upper 100 dbar to a roughly 300-dbar thick layer just below, as described in last year's report (Johnson et al. 2018). In 2018, as in 2017, the entire water column measured by Argo was visibly warmer than the 2004–18 average (Fig. 3.5a). However, in 2018, the waters from 0 dbar to 100 dbar were less warm than in 2017, with a maximum difference of about −0.06°C near the surface, consistent with the SST analysis (Section 3.3a). In contrast, the waters below (around 100–1000 m) were warmer, with a maximum difference of about +0.06°C near 160 dbar, and another local maximum difference of 0.01°C near 600 dbar. This vertical redistribution may be partly due to the very strong 2016/17 El Niño (e.g., Johnson and Birnbaum 2017). However, as noted below, the net effect was that the water column from 0–2000 m gained a substantial amount of heat from 2017 to 2018. The overall warming trend (Fig. 3.5b, orange line) from 2004 to 2018 exceeds 0.18°C decade^{-1} near the surface, declining to less than 0.03°C decade^{-1} below 300 dbar and about 0.01°C decade^{-1} by 2000 dbar. As noted in previous reports, removing a linear regression against the Niño3.4 index (e.g., Johnson and Birnbaum 2017) results in a decadal warming trend (Fig. 3.5b, blue line) that is slightly smaller, at about 0.16°C decade^{-1}, near the surface and slightly larger than the simple linear trend from about 100 dbar to 1600 dbar. This difference is because of the influence of the 2016/17 El Niño near the end of the relatively short record.

The analysis is extended back in time from the Argo period to 1993, and deeper, using sparser, more heterogeneous historical data collected mostly from ships (e.g., Abraham et al. 2013). The six different estimates of annual globally integrated in situ 0–700-m OHCA (Fig. 3.6a) all reveal a large increase since 1993, with five of the analyses reporting 2018 as a record high. The globally integrated 700–2000-m OHCA annual values (Fig. 3.6b) vary more among analyses, and only two report 2018 as a record high, but the long-term warming trend in this layer is also clear. Globally integrated OHCA values in both layers vary more both from year-to-year for individual years and from estimate-to-estimate in any given year prior to the achievement of a near-global Argo array around 2005. Causes of differences among estimates are discussed in Johnson et al. (2015).

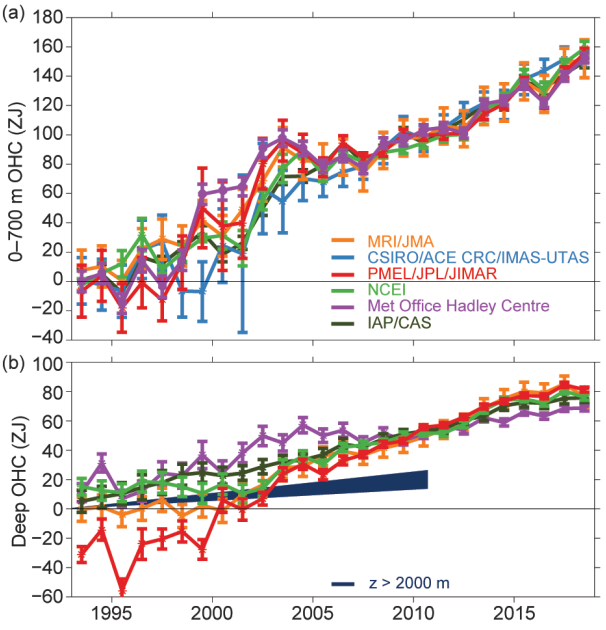

Fig. 3.6. (a) Annual average global integrals of in situ estimates of upper (0–700 m) OHCA (ZJ; 1 ZJ = 10^{21} J) for 1993–2018 with standard errors of the mean. The MRI/JMA estimate is an update of Ishii et al. (2017). The CSIRO/ACE CRC/IMAS-UTAS estimate is an update of Domingues et al. (2008). The PMEL/JPL/JIMAR estimate is an update and refinement of Lyman and Johnson (2014). The NCEI estimate follows Levitus et al. (2012). The Met Office Hadley Centre estimate is computed from gridded monthly temperature anomalies (relative to 1950–2018) following Palmer et al. (2007). The IAP/CAS estimate is an update of that reported in Cheng and Zhu (2018). See Johnson et al. (2014) for details on uncertainties, methods, and datasets. For comparison, all estimates have been individually offset (vertically on the plot), first to their individual 2005–18 means (the best sampled time period), and then to their collective 1993 mean. (b) Annual average global integrals of in situ estimates of intermediate (700–2000 m) OHCA for 1993–2018 with standard errors of the mean, and a long-term trend with one standard error uncertainty shown from 1992–2010 for deep and abyssal (z > 2000 m) OHCA following Purkey and Johnson (2010) but updated using all repeat hydrographic section data available from https://cchdo.ucsd.edu/ as of December 2018.

The rate of heat gain from linear fits to each of the six global integral estimates of 0–700 m OHCA from 1993 through 2018 (Fig. 3.6a) ranges from 0.36 (±0.06) to 0.42 (±0.06) W m^{-2} applied over the surface area of Earth (Table 3.2). Linear trends from 700 m to 2000 m over the same time period range from 0.14 (±0.05) to 0.32 (±0.03) W m^{-2}. Trends in the 0–700-m layer all agree within uncertainties, but one of the trends in the 700–2000-m layer, which is quite sparsely sampled prior to the start of the Argo

era (circa 2005), does not. It is likely the different methods for dealing with under-sampled regions in analyses cause the disagreement in the long-term trends for the 700–2000-m layer OHCA estimates. For 2000–6000 m, the linear trend is 0.07 (±0.04) W m^{-2} from September 1992 to May 2011, using repeat hydrographic section data collected from 1981 to 2018 to update the estimate of Purkey and Johnson (2010). Summing the three layers (with their slightly different time periods), the full-depth ocean heat gain rate ranges from 0.57 to 0.81 W m^{-2} roughly applicable to 1993–2018. Estimates starting circa 2005 have much smaller uncertainties, e.g., 0.61 ± 0.09 W m^{-2} for ocean warming at depths of 0–1800 dbar during 2005–15 (Johnson et al. 2016).

Table 3.2. Trends of ocean heat content increase (in W m^{-2} applied over the 5.1 × 10^{14} m^2 surface area of Earth) from seven different research groups over three depth ranges (see Fig. 3.6 for details). For the 0–700- and 700–2000-m depth ranges, estimates cover 1993–2018, with 5%–95% uncertainties based on the residuals taking their temporal correlation into account when estimating degrees of freedom (Von Storch and Zwiers 1999). The 2000–6000-m depth range estimate, an update of Purkey and Johnson (2010), uses data from 1981 to 2018, but the globally averaged first and last years are 1992.7 and 2011.4, again with 5%–95% uncertainty.

Research group	Global ocean heat content trends (W m^{-2}) for three depth ranges		
	0–700 m	700–2000 m	2000–6000 m
MRI/JMA	0.36 ± 0.06	0.24 ± 0.05	—
CSIRO/ACE/CRC/IMAS/UTAS	0.42 ± 0.06	—	—
PMEL/JPL/JIMAR	0.39 ± 0.14	0.32 ± 0.03	—
NCEI	0.38 ± 0.06	0.19 ± 0.06	—
Met Office Hadley Centre	0.36± 0.15	0.14 ± 0.05	—
IAP/CAS	0.39 ± 0.05	0.18 ± 0.02	—
Purkey and Johnson update	—	—	0.07 ± 0.04

d. Salinity—G. C. Johnson, J. Reagan, J. M. Lyman, T. Boyer, C. Schmid, and R. Locarnini

1) Introduction—G. C. Johnson and J. Reagan

Salinity is the fraction of dissolved salts in water, nominally in g kg^{-1}, but measured and reported here as a dimensionless quantity on the 1978 Practical Salinity Scale, or PSS-78 (Fofonoff and Lewis 1979). Salinity and temperature together determine the density of seawater at a given pressure. Their variability can alter the density patterns that are integral to the global thermohaline circulation (e.g., Gordon 1986; Broecker 1991). One prominent limb of the global thermohaline circulation, the AMOC, is particularly susceptible to changes in salinity (e.g., Liu et al. 2017). Salinity is also a conservative water property, traceable back to where a water mass was originally formed at the surface and subducted into the ocean's interior (e.g., Skliris et al. 2014). Where precipitation dominates evaporation, fresher surface seawater is found (i.e., along the ITCZ and at high latitudes), and where evaporation dominates precipitation, saltier surface seawater is found (i.e., in the subtropics). Salinity acts as a natural rain gauge (e.g., Terray et al. 2012), useful since ~80% of the global hydrological cycle takes place over the ocean (e.g., Durack 2015). Salinity changes are used to estimate changes in the hydrological cycle (e.g., Durack et al. 2012). They also play a role in local sea level changes through seawater contraction with salinification and expansion with freshening (e.g., Durack et al. 2014). Finally, besides atmospheric freshwater fluxes, other factors can modify salinity such as advection, mixing, entrainment, sea ice melt/freeze, and river runoff (e.g., Ren et al. 2011).

Different data sources are used for different salinity analyses in this section owing to data availability and accuracy. To investigate interannual changes of subsurface salinity, all available salinity profile data are quality controlled following Boyer et al. (2013) and then used to derive 1° monthly mean gridded salinity anomalies relative to a long-term monthly mean for years 1955–2012 [World Ocean Atlas 2013 version 2 (WOA13v2); Zweng et al. 2013] at standard depths from the surface to 2000 m (Boyer et al. 2013). In recent years, the largest source of salinity profiles is the Argo program (Riser et al. 2016). These data are a mix of real-time (preliminary) and delayed-mode (scientific quality controlled) observations. Hence, the estimates presented here could change after all data are subjected to scientific quality control. The sea surface salinity (SSS) analysis relies on Argo data downloaded in January 2019, with annual maps generated following Johnson and Lyman (2012) as well as monthly maps of bulk (as opposed to skin) SSS data from the Blended Analysis of Surface Salinity (BASS) (Xie et al. 2014). BASS blends in situ SSS data with data from the Aquarius (Le Vine et al. 2014; mission ended in June 2015), Soil Moisture and Ocean Salinity

(SMOS; Font et al. 2013), and recently Soil Moisture Active Passive (SMAP; Fore et al. 2016) satellite missions. BASS maps can be biased fresh around land (including islands), and features at high latitudes should be validated with in situ maps. Despite the larger uncertainties of satellite data relative to Argo data, their higher spatial and temporal sampling allows higher spatial and temporal resolution maps than are possible using in situ data alone at present.

2) Sea surface salinity—G. C. Johnson and J. M. Lyman

Extratropical 2018 SSS anomalies (Fig. 3.7a, colors) exhibit large-scale similarities with those from 2004 to 2017 (see previous *State of the Climate* reports). With the partial exception of the North Pacific in 2018 and 2017, subtropical salinity maxima are mostly salty with respect to the WOA13v2 climatology. The fresher higher latitude regions such as the subpolar North Pacific, the Irminger and portions of the Nordic seas of the North Atlantic, and some portions of the Southern Ocean are anomalously fresh with respect to climatology. A warmer atmosphere can hold more water, withdrawing more in evaporative regions and depositing more in precipitation-prone regions, which would lead to the salinity patterns observed (Rhein et al. 2013), as well as those seen in the extratropical 2005–18 trends discussed below. Within the tropics, which have large SSS excursions with ENSO and other interannual variations, both the ITCZ and SPCZ in the Pacific are quite fresh in 2018 with respect to climatology (Fig. 3.7a), as is the region near the Amazon and Orinoco river mouths in the Atlantic.

A tight relationship between anomalies of air–sea freshwater fluxes (precipitation minus evaporation; $P - E$) and SSS anomalies is especially apparent in the year-to-year changes of both quantities. Where SSS changes from 2017 to 2018 (Fig. 3.7b, colors) are positive, $P - E$ tendencies over that same period are often negative (see Fig. 3.12b). With a reduction in rainfall from 2017 to 2018 around the Maritime Continent, that region between the Indian and Pacific Oceans sees an increase in SSS from 2017 to 2018. With increased freshwater flux into the ocean around the Pacific ITCZ, the SSS in the region decreases from 2017 to 2018, whereas south of the equator the opposite pattern holds. This relationship can also be seen in the freshening tropical Indian Ocean, the salinifying subtropical North Pacific, and the freshening Gulf of Alaska, among other regions. The freshening SSS tendency from 2017 to 2018 just south of the equator in the Indian Ocean may be partly owing to an increase in anomalous westward currents between

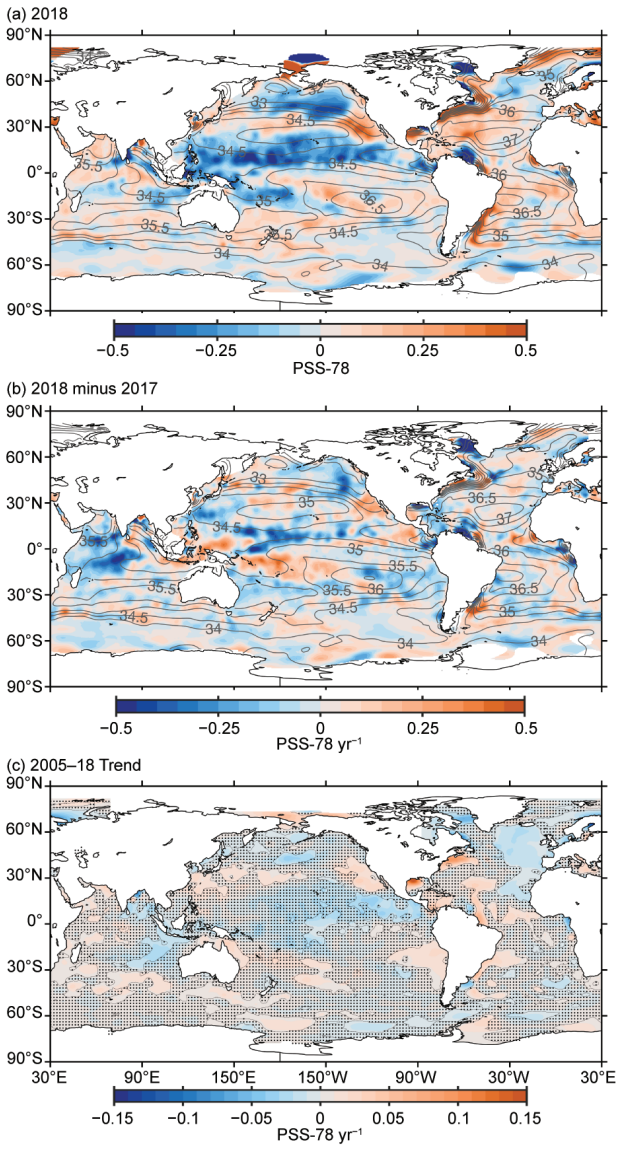

Fig. 3.7. (a) Map of the 2018 annual surface salinity anomaly (colors, PSS-78) with respect to monthly climatological 1955–2012 salinity fields from WOA13v2 (yearly average—gray contours at 0.5 intervals, PSS-78). (b) Difference of 2018 and 2017 surface salinity maps (colors, PSS-78 yr^{-1}). White ocean areas are too data-poor (retaining < 80% of a large-scale signal) to map. (c) Map of local linear trends estimated from annual surface salinity anomalies for 2005–18 (colors, PSS-78 yr^{-1}). Areas with statistically insignificant trends at 5%–95% confidence are stippled. All maps are made using Argo data downloaded in January 2019.

2017 and 2018 there (see Fig. 3.18b) in the presence of mean SSS that increases from east to west.

As in 2017, strong seasonal variations of BASS (Xie et al. 2014) SSS anomalies (Fig. 3.8) are evident near the Amazon and Orinoco River plumes in 2018. For the first three quarters of the year, there is a fresh anomaly localized near the coast, but it extends east-

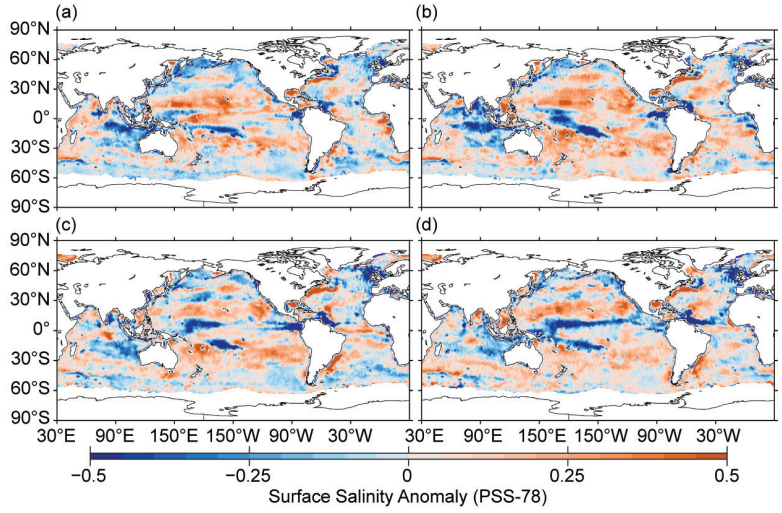

Fig. 3.8. Seasonal maps of SSS anomalies (colors) from monthly blended maps of satellite and in situ salinity data (BASS; Xie et al. 2014) relative to monthly climatological 1955–2012 salinity fields from WOA13v2 for (a) Dec–Feb 2017/18, (b) Mar–May 2018, (c) Jun–Aug 2018, and (d) Sep–Nov 2018. Areas with maximum monthly errors exceeding 10 PSS-78 are left white.

ward across much of the northern equatorial Atlantic in September–November. In the tropical Pacific, a fresh anomaly builds under the ITCZ in June–August and strengthens in September–November.

Sea surface salinity trends for 2005–18, the era of near-global Argo coverage, are estimated by local linear fits to annual average SSS maps from Argo data (Fig. 3.7c). Large-scale patterns of local trends have not changed much from last year's report. Regions with already high salinity values, such as the subtropical salinity maxima in all the ocean basins and the Arabian Sea, show increasing trends, with statistical significance in some portions of those regions, especially in the South Indian Ocean and in the Pacific off the west coasts of the Americas. Statistically significant freshening trends are apparent in the subpolar North Pacific, the eastern subpolar North Atlantic, the eastern warm fresh pool in the tropical North Pacific, and the Bay of Bengal. These are all regions that are climatologically fresh relative to their surroundings. In the Gulf of Mexico and along the east coast of North America from roughly Cape Hatteras northward, strong, statistically significant trends toward saltier and warmer (section 3c) conditions are evident.

3) Subsurface salinity—J. Reagan, T. Boyer, C. Schmid, and R. Locarnini

The 2009–18 basin-average monthly salinity anomalies (Fig. 3.9a) for the Atlantic Ocean continued the same pattern that has been evident for the past decade, with weak anomalies (< |0.005|) below ~600 m and salty anomalies (> 0.005) extending and increasing from ~600 m to the surface where they reach values exceeding 0.05. There is freshening (~ −0.015) between 2017 and 2018 in the upper 50 m with salinification extending from 100 m to 1200 m and a maximum (~0.01) around 150 m (Fig. 3.9b). The deeper (250–700 m) salinification tendency in 2018 may be related to the deepening of the salinity anomalies from 2017 (Fig. 3.9a). 2018 is also the first year in the past decade when all 0–1500-m basin-average monthly salinity anomalies were saltier than the long-term mean (Fig. 3.9a).

The 2018 Pacific Ocean basin-average monthly salinity anomalies for 0–1500 m continued the same pattern that has been evident since mid-2014 (Fig. 3.9c). There are fresh anomalies in the upper 100 m, salty anomalies from 100–250 m, fresh anomalies from 275–600 m, and weak (< |0.005|) anomalies at depths below 600 m (Fig. 3.9c). Changes from 2017 to 2018 (Fig. 3.9d) include freshening in the upper ~100 m (max of ~−0.015 at 50 m) and salinification from 125–375 m (max of ~0.015 at 200 m). These tendencies are very similar to what was seen between 2016 and 2017 (see Fig. 3.9d in Reagan et al. 2018). 2018 also marks the fourth straight year with fresh anomalies in the upper 100 m, following a 5-year period (2009–14) of persistent salty anomalies in the upper 100 m (Fig. 3.9c). A possible cause for these persistent anomalies may be related to in-phase transitions of ENSO and PDO (see discussion in Reagan et al. 2018).

The Indian Ocean basin-average monthly salinity anomalies experienced persistent fresh anomalies in the upper 0–100/200 m from mid-2011 through mid-2016, with salty anomalies in a 100–200-m thick layer below (Fig. 3.9e). The 0–100-m salinity exceeded the long-term average in mid-2016 through early 2018, followed by some near-surface (< 50 m) freshening evident in mid-2018. There are also salty anomalies extending from the surface to depths of ~700 m during the latter half of 2018 (Fig. 3.9e). The major change between 2017 and 2018 was very strong freshening (< ~−0.025) in the upper 30 m (Fig. 3.9f), discussed further below.

The zonally-averaged salinity tendency from 2017 to 2018 in the upper 500 m of the Atlantic Ocean shows strong freshening in the upper 50 m along the

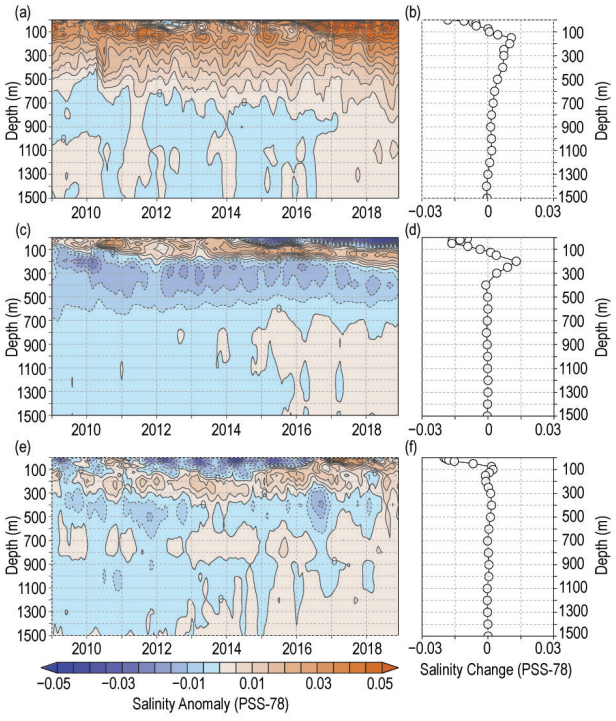

Fig. 3.9. Average monthly salinity anomalies from 0–1500 m for the (a) Atlantic from 2009–18 and (b) the change from 2017 to 2018; (c) Pacific from 2009–18 and (d) the change from 2017 to 2018; (e) Indian from 2009–18 and (f) the change from 2017 to 2018. Data were smoothed using a 3-month running mean. Anomalies are relative to the long-term WOA13v2 monthly salinity climatology for years 1955–2012 (Zweng et al. 2013).

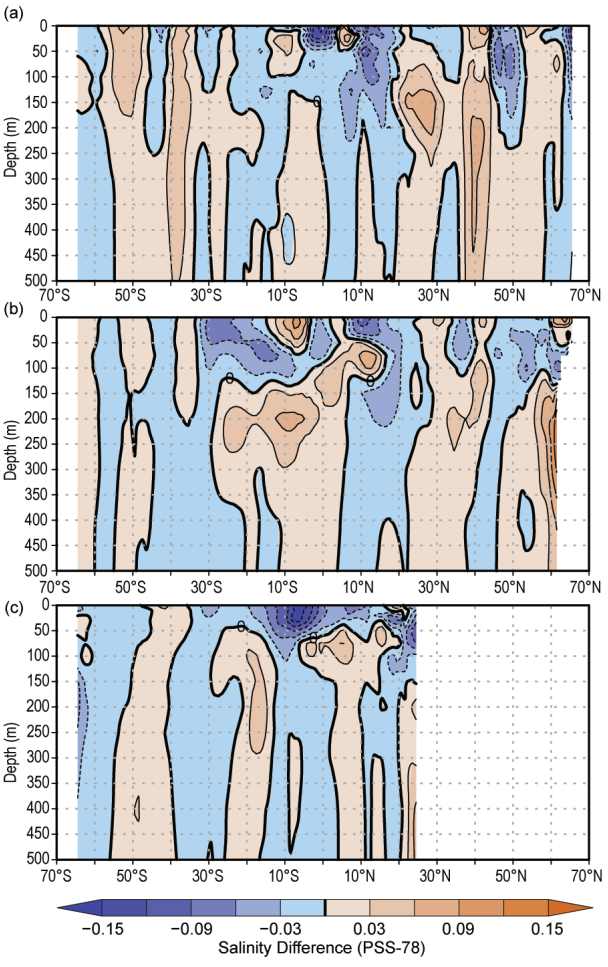

Fig. 3.10. Difference between the 2018 and 2017 zonal average monthly salinity anomalies from 0–500m for the (a) Atlantic, (b) Pacific, and (c) Indian Ocean basins. Anomalies are relative to the long-term WOA13v2 monthly salinity climatology for years 1955–2012 (Zweng et al. 2013). Contours represent multiples of ±0.03 with a bold 0 contour.

equator (max < −0.15 at 0 m, Fig. 3.10a) which is associated with a narrow strip of near-surface freshening between the Gulf of Guinea and Northeast Brazil (Fig. 3.7b). Additionally, there is freshening (< −0.03) from 10°N to −20°N extending from 0 m to 200 m. There is also freshening from 45°N to 52°N in the upper 150 m, which is opposite to the salinification observed between 2016 and 2017 (see Fig. 3.10a in Reagan et al. 2018). Finally, there is salinification (> 0.03) from 0 m to 500 m near 40°N and 40°S, from 0 m to 175 m between 48°–55°S, and a subsurface area from 20°–30°N at 75–250 m (Fig. 3.10a).

The changes in the Pacific Ocean zonally-averaged salinity from 2017 to 2018 are mainly confined to the upper 300 m (Fig. 3.10b). There is freshening (< −0.03) from 18°–32°S and 0–75 m that deepens northward to 10°S and 100 m, freshening from 8°N to 16°N and 0–40 m, and salinification from 4°–12°S and 0–50 m. The latter freshening and salinification tendencies are likely associated with changes in oceanic freshwater gains and losses from evaporation and precipitation (see Fig. 3.12b). All of the aforementioned freshening and salinification tendencies shifted southward from where they were located the previous year (see Fig. 3.10b in Reagan et al. 2018). Finally, there was also salinification (> 0.03) in two subsurface Pacific regions, one centered at 10°S and 200 m and the other at greater depths between 125–500 m northward of 55°N.

Much of the larger changes (> |0.03|) of the zonally averaged salinity anomalies from 2017 to 2018 in the Indian Ocean occurred in the upper 100 m (Fig. 3.10c). There was freshening from 20°S to 10°N in the 0–50 m layer, which is a complete reversal of the prominent salinification observed there between 2016 and 2017 (see Fig. 3.10c in Reagan et al. 2018). This freshening may be due to anomalous westward surface currents (see Fig. 3.18b) in the equatorial Indian Ocean transporting fresher water westward, a reversal from what was observed last year (Johnson

and Lyman 2018). Much of this freshening is located in the Arabian Sea and the central and western portions of the tropical Indian Ocean, northward of 15°S (Fig. 3.8b). There is also freshening in the upper 150 m northward of 20°N from 2017 to 2018.

e. *Global ocean heat, freshwater, and momentum fluxes*—L. Yu, X. Jin, P. W. Stackhouse, A. C. Wilber, S. Kato, N. G. Loeb, and R. A. Weller

The ocean and the atmosphere communicate via interfacial exchanges of heat, freshwater, and momentum. These air–sea fluxes are the primary mechanisms for keeping the global climate system in near balance with the incoming insolation at Earth's surface. Most of the shortwave radiation (SW) absorbed by the ocean's surface is vented into the atmosphere by three processes: longwave radiation (LW), turbulent heat loss by evaporation (latent heat flux, or LH), and by conduction (sensible heat flux, or SH). The residual heat is stored in the ocean and transported away by the ocean's surface circulation, forced primarily by the momentum transferred to the ocean by wind stress. Evaporation connects heat and moisture transfers, and the latter, together with precipitation, determines the local surface freshwater flux. Identifying changes in the air–sea fluxes is essential in deciphering observed changes in ocean circulation and its transport of heat and salt from the tropics to the poles.

Air–sea heat flux, freshwater flux, and wind stress in 2018 and their relationships with ocean surface variables are examined here. The net surface heat flux, Q_{net}, is the sum of four terms: SW + LW + LH + SH. The net surface freshwater flux into the ocean (neglecting riverine and glacial fluxes from land) is simply Precipitation (P) minus Evaporation (E), or the $P - E$ flux. Wind stress is computed from satellite wind retrievals using the bulk parameterization of Edson et al. (2013). The production of the global maps of Q_{net}, $P - E$, and wind stress (Figs. 3.11–3.13) and the long-term perspective of the change of the forcing functions (Fig. 3.14) is made possible through integrating multi-group efforts. Ocean-surface LH, SH, E, and wind stress are from the OAFlux project's newly developed satellite-derived, high-resolution (hereafter OAFlux-HR) products (Yu and Jin 2014; Yu 2019). Surface SW and LW radiative fluxes are from the CERES Fast Longwave And Shortwave Radiative Fluxes (FLASHFlux) Ed3A product (Stackhouse et al. 2006). Global P is from the GPCP version 2.3 products (Adler et al. 2003). The CERES Energy Balanced and Filled (EBAF) surface SW and LW version 4.0 products (Loeb et al. 2018; Kato et al. 2018) are used in the time series analysis.

1) Surface heat fluxes

The dominant features in the 2018 Q_{net} anomaly field (Fig. 3.11a) are the broad-scale oceanic heat gain (positive Q_{net} anomalies) in the equatorial and southern Pacific and Indian Oceans (40°S–10°N), and the oceanic heat loss (negative Q_{net} anomalies) in the subtropical North Pacific (10°–30°N), the North Atlantic (10°–60°N), and the southern higher latitudes (40°S poleward). Positive and negative anomalies both exceeded 25 W m^{-2}. The 2018-minus-2017 Q_{net} tendency field (Fig. 3.11b) was predominantly determined by the LH + SH change pattern. The spatial pattern of Q_{net} tendencies is similar to that of the 2018-minus-2017 anomaly pattern (Fig. 3.11b) over most of the global ocean, showing that the 2018 anomalies were a strong departure from the climatological mean state. However, the two patterns differ considerably

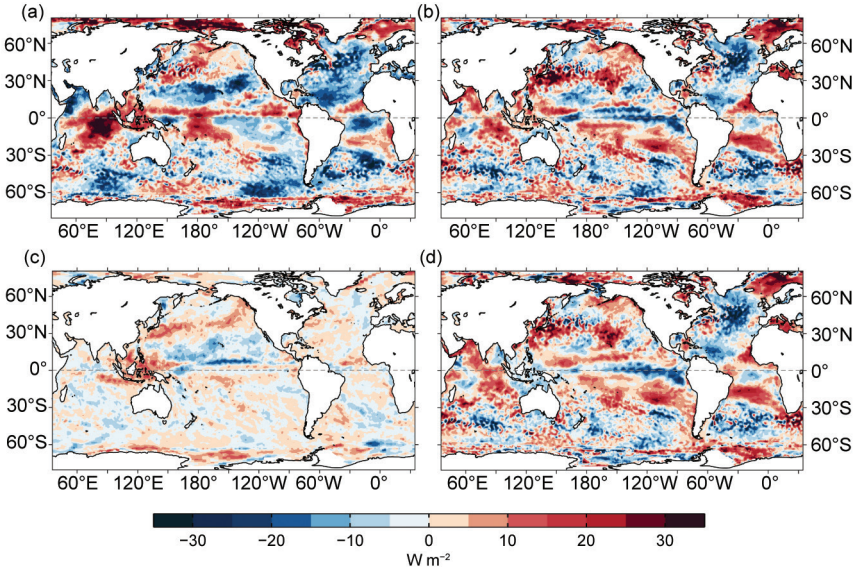

Fig. 3.11. (a) Surface heat flux (Q_{net}) anomalies (W m^{-2}) for 2018 relative to a 5-yr (2010–14) mean. Positive values denote ocean heat gain. (b) 2018 minus 2017 tendency for Q_{net}, (c) surface radiation (SW+LW), and (d) turbulent heat fluxes (LH+SH), respectively. Positive tendencies denote more ocean heat gain in 2018 than in 2017, consistent with the reversal of the color scheme in (d). LH+SH are produced by the OAFlux high-resolution (HR) satellite-based analysis, and SW+LW by the NASA FLASHFlux project.

in a few regions, most notably the tropical Pacific where the 2018 tendencies have signs opposite to the 2018 anomalies. Note that the net heat loss tendencies south of 60°S may be influenced by sea–ice edge effect on flux estimates.

The tropical Pacific returned to ENSO-neutral conditions after a weak La Niña ended in March 2018 (see section 4b). There was a widespread sea-surface cooling tendency over most of the equatorial ocean with the exception of a weak warming tendency in the central equatorial Pacific (Fig. 3.1). The 2018 LH+SH tendencies (Fig. 3.11d) show a large increase in the central and eastern equatorial region (positive LH+SH anomalies, blue colors) and a substantial reduction south of the equator (negative LH+SH anomalies, red colors). Note that the color scheme is reversed to indicate that increased LH+SH (positive anomalies, blue colors) have a cooling effect on the ocean surface and, conversely, reduced LH+SH (negative anomalies, red colors) have a warming effect. The 2018 SW+LW tendencies (Fig. 3.11c) show less radiative heat input to the ocean in 2018 than in 2017 to the north of the equatorial Pacific and more radiative heat input to the south, with a maximum reduction occurring in the central basin under the ITCZ and a maximum enhancement occurring in the far western equatorial Pacific and the Maritime Continent. Outside of the equatorial ocean, a zonal band of larger SW+LW tendencies (>10 W m^{-2}) in the mid-latitude North Pacific extended from the Kuroshio Extension northeastward to the Gulf of Alaska. SW+LW tendencies were small (<5 W m^{-2}) elsewhere.

In the Northeast Pacific, the "Warm Blob" (Bond et al. 2015) reemerged in June 2018 (Fig. 3.2), featuring a large mass of warmer water underneath a higher-than-normal pressure zone off North America's west coast and particularly noted in the Gulf of Alaska. Under the higher-pressure system, surface radiative heat input increased (positive SW+LW tendencies, Fig. 3.11c) due to the reduction of clouds and reduced surface turbulent heat loss (LH+SH negative anomalies, Fig. 3.11d) due to wind weakening (Fig. 3.13b). Both SW+LW and SH+LH tendencies had a warming effect on the ocean surface. The radiative and turbulent heat flux tendencies also created a warming effect in the vicinity of the Kuroshio Extension.

In the North Atlantic, the cooling effect of LH+SH tendencies dominated over the warming effect of SW+LW tendencies. A strong positive NAO index persisted from December 2017 through October 2018, then showed a transition to neutral phase. Surface winds were intensified significantly in 2018 (Fig. 3.13b), leading to pronounced turbulent heat loss (positive LH+SH tendencies, blue color) over the basin from the equator to 60°N latitude. In the equatorial and south subtropical Atlantic, LH+SH tendencies produced a warming effect; this appears to be associated with wind weakening in these regions.

In the Indian Ocean, a positive dipole event occurred during September–November. Albeit short lived, both SW+LW and LH+SH tendencies displayed a dipole-like pattern in the equatorial zone. In the east, SW+LW increased and LH+SH reduced, which combined to produce a marked increase of heat gain at the ocean surface (positive Q_{net} tendencies). In the central equatorial basin, there was a slight reduction in SW+LW and a slight increase in LH+SH, giving rise to a slight increase of heat loss at the ocean surface (negative Q_{net} tendencies).

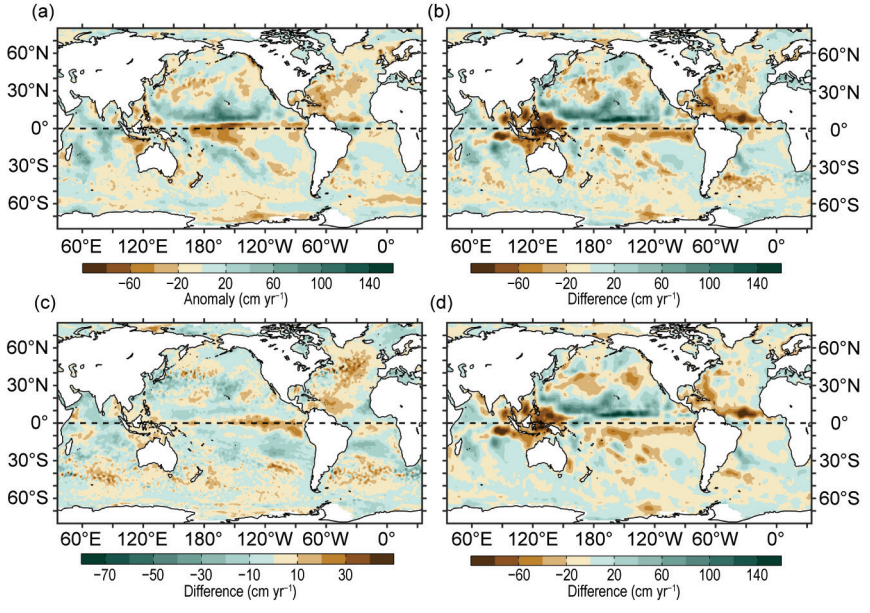

Fig. 3.12 (a) Surface freshwater (*P* − *E*) flux anomalies (cm yr^{-1}) for 2018 relative to the 1988–2014 climatology. 2018 minus 2017 tendencies for (b) *P* − *E*, (c) evaporation (*E*), and (d) precipitation (*P*). Green colors denote anomalous ocean moisture gain, and browns denote loss, consistent with the reversal of the color scheme in (c). *P* is computed from the GPCP version 2.3 product, and *E* from OAFlux-HR.

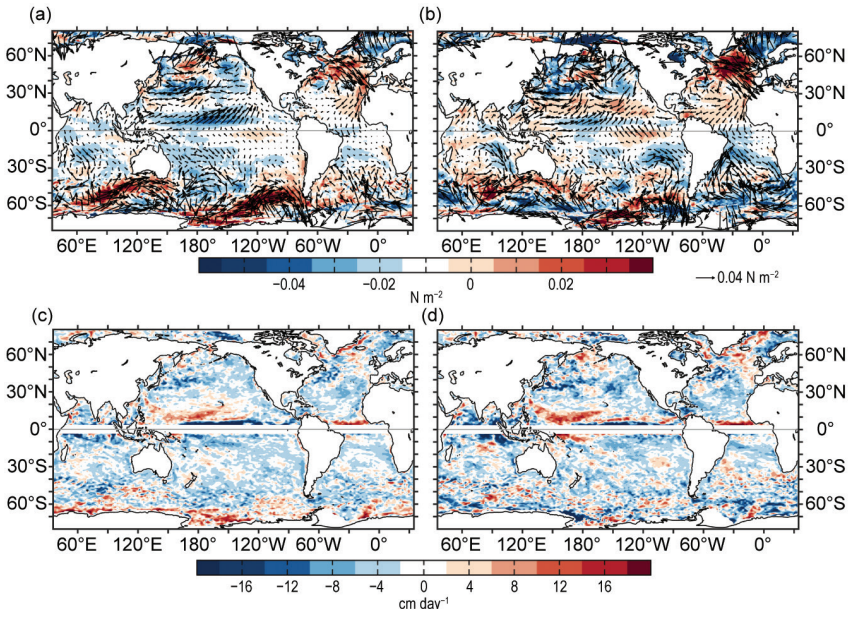

Fig. 3.13. (a) Wind stress magnitude (colors) and vector anomalies (N m^{-2}) for 2018 relative to the1988–2014 climatology, (b) 2018 minus 2017 tendencies in wind stress, (c) Ekman vertical velocity (W_{EK}; cm day^{-1}) anomalies for 2018 relative to the 1988–2014 climatology, and (d) 2018 minus 2017 tendencies in W_{EK}. In (c) and (d), positive values denote upwelling tendency, and negative downwelling tendency. Winds are computed from the OAFlux-HR.

2) Surface freshwater fluxes

The 2018 $P - E$ anomaly pattern shows that net freshwater input at the ocean surface increased in the north tropical Pacific and the tropical Indian Ocean (positive anomalies, green colors) but decreased in the south tropical Pacific and mid-latitudes in both Northern and Southern Hemispheres (negative anomalies, brown colors) (Figs. 3.12a). A similar global pattern is also shown in the 2018 $P - E$ tendencies (Fig. 3.12b) with the exception of the equatorial Pacific, where $P - E$ negative anomalies were more oriented to the south of the equator in the central and eastern basin. The tropical $P - E$ tendencies are attributable to the P tendencies (Fig. 3.12d) and are consistent with the SW+LW tendencies. The tropical SW+LW tended to decrease in areas of increased ITCZ rainfall and to increase in area of reduced ITCZ rainfall.

The E tendencies (Fig. 3.12c) show that ocean evaporation increased in the equatorial Pacific and Atlantic Oceans and also at mid latitudes (30°–60° north and south). The increase of E was most pronounced in the North Atlantic, spanning latitudes from the equator to 60°N. Coherent drying tendencies were also evident in the P flux, indicating that the North Atlantic had a deficit in surface freshwater input in 2018.

The largest drying tendencies in the P flux occurred in the far western equatorial Pacific and the eastern equatorial Indian Ocean, with maximum magnitude exceeding 45 cm from 2017 to 2018. The P tendencies also display a dipole-like pattern in the tropical Indian Ocean, with reduced freshwater input (drying) in the east and enhanced freshwater input (wetting) in the west. In the Gulf of Alaska where Q_{net} increased coinciding with the return of the "Warm Blob," $P - E$ increased, and it decreased to the south.

3) Wind stress

The 2018 wind stress anomaly pattern (Fig. 3.13a) indicates that the trade winds weakened north of the equator and strengthened south of the equator in the tropical Pacific with respect to climatology. Marked increase of westerly winds is evident in the mid-latitude North Pacific and Atlantic (50°–60°N) and along the Antarctic Circumpolar Current (ACC) in the Southern Ocean (40°–60°S). Strengthening of surface winds in the North Atlantic associated with the positive NAO event is clear in the 2018 tendency map (Fig. 3.13b), as is the weakening of surface winds in the northeast Pacific associated with the "Warm Blob." The strong wind tendencies were the primary cause of the large turbulent heat loss tendencies in the eastern equatorial Pacific and North Atlantic.

Winds vary considerably in space. This causes divergence and convergence of the Ekman transport, leading to a vertical velocity, denoted by Ekman pumping (downward) or suction (upward) velocity W_{EK}, at the base of the Ekman layer. Computation of W_{EK} follows the equation: $W_{EK} = 1/\rho\nabla\times(\tau/f)$, where ρ is the density, τ is the wind stress, and f the Coriolis force. The 2018 W_{EK} tendencies (Fig. 3.13d) show upwelling (positive) anomalies in the vicinity of the ITCZ (3°–7°N) in the equatorial Pacific and Atlantic and downwelling (negative) anomalies in the equatorial Indian Ocean. Outside of the tropical region, the strengthened westerly band in the mid-latitude North Pacific induced a band of downwelling anomalies (negative) to the south. In the North Atlantic, W_{EK} anomalies were characterized

by negative downwelling anomalies in the low-mid latitudes (0–50°N) and positive upwelling anomalies at higher latitudes (50°–60°N). Negative downwelling anomalies predominated the ocean basins in the Southern Hemisphere.

4) Long-term perspective

A long-term perspective on the change of ocean-surface forcing functions in 2018 is assessed in the context of multi-decade annual-mean time series of Q_{net}, $P - E$, and wind stress averaged over the global ice-free oceans (Figs.3.14a–c). The Q_{net} time series commenced in 2001, when CERES EBAF4.0 surface radiation products became available. The $P - E$ and wind stress time series are each 30 years long, starting from 1988 when higher quality global flux fields can be constructed from SSM/I satellite retrievals. Q_{net} anomalies are relative to the 2001–15 climatology, and $P - E$ and wind stress anomalies are relative to the 1988–2015 period.

Q_{net} remained relatively level between 2001 and 2007, but after a sharp dip in 2008, it underwent a steady increase and peaked in 2016. In general, the ocean surface has received more heat from the atmosphere in recent years. The 2018 Q_{net} was a slight increase from the sharp reduction in 2017. The 30-year records of $P - E$ and wind stress show a regime shift around 1999. The downward trend in $P - E$ and upward trend in wind stress that dominated the 1990s have flattened since 1999, and the 2018 conditions continued weak interannual fluctuations.

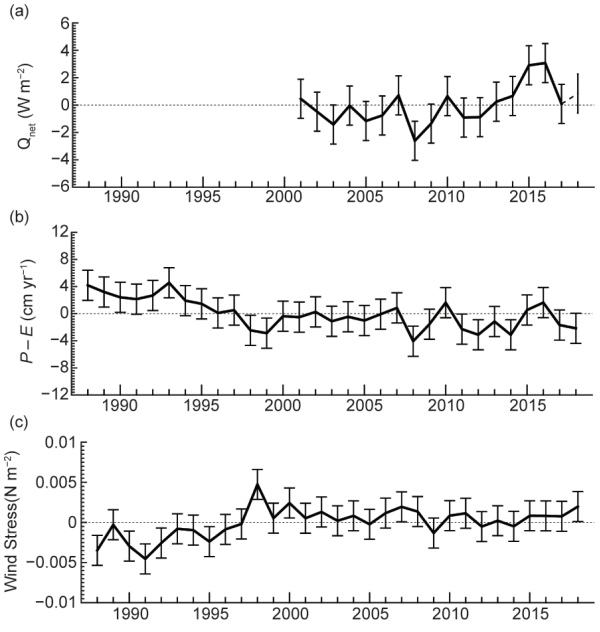

Fig. 3.14. Annual-mean time series of global averages of (a) net surface heat flux (Q_{net}; W m^{-2}) from the combination of CERES EBAF4.0 SW+LW and OAFlux-HR LH+SH. The 2018 Q_{net} estimate is based on FLASHFlux and OAFlux-HR. (b) net freshwater flux ($P - E$; cm yr^{-1}) from the combination of GPCP *P* and OAFlux-HR *E*, and (c) wind stress magnitude (N m^{-2}) from OAFlux-HR. The error bars denote one standard deviation of annual-mean variability.

f. Sea level variability and change—P. R. Thompson, M. J. Widlansky, E. Leuliette, W. Sweet, D. P. Chambers, B. D. Hamlington, S. Jevrejeva, J. J. Marra, M. A. Merrifield, G. T. Mitchum, and R. S. Nerem

Global mean sea level (GMSL) during 2018 was the highest annual average in the satellite altimetry record (1993–present), rising to 81 mm (3.2 in) above the 1993 average (Fig. 3.15a). This marks the seventh consecutive year (and 23rd of the last 25) that GMSL increased

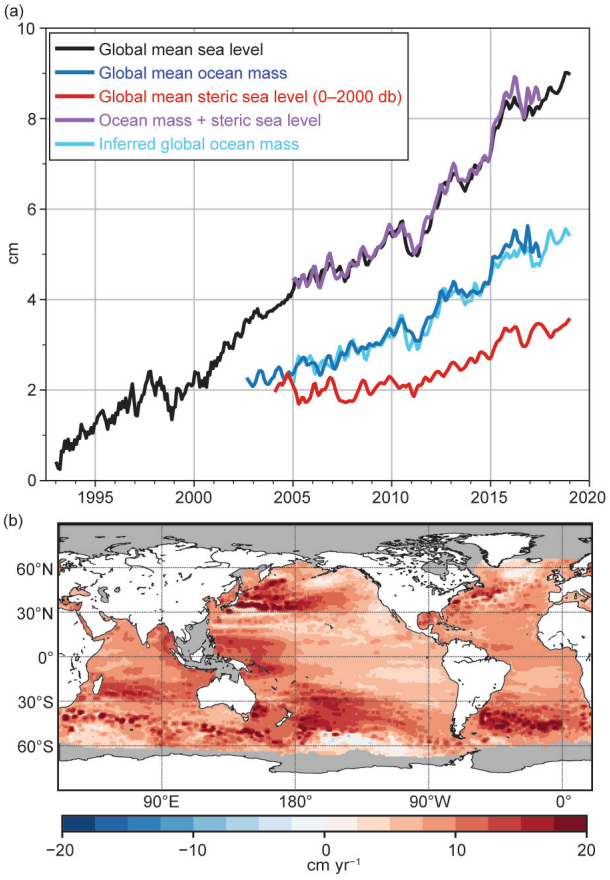

Fig. 3.15. (a) [black] Monthly averaged global mean sea level observed by satellite altimeters (1993–2018 from the NOAA Laboratory for Satellite Altimetry). [blue] Monthly averaged global ocean mass (2003–August 2017 from the Gravity Recovery and Climate Experiment). [red] Monthly averaged global mean steric sea level (2004–18) from the Argo profiling float array. [purple] Mass plus steric. [cyan] Inferred global ocean mass calculated by subtracting global mean steric sea level from global mean sea level. All time series have been smoothed with a 3-month filter. (b) Total local sea level change from altimetry during 1993–2018.

relative to the previous year. The new high reflects an ongoing multi-decadal trend in GMSL during the satellite altimetry era, 3.1 ± 0.4 mm yr^{-1} (Fig. 3.15a). Acceleration in GMSL (i.e., two times the quadratic coefficient in a second-order polynomial fit) during the altimetry era is 0.097 ± 0.04 mm yr^{-2}. When effects of the Pinatubo volcanic eruption and ENSO are subtracted from GMSL variability, the estimated climate-change-driven acceleration in GMSL over the altimeter record is 0.084 ± 0.025 mm yr^{-2} (Nerem et al. 2018).

Variations in GMSL (Fig. 3.15a) result from changes in both the mass and density of the global ocean (Leuliette and Willis 2011; Cazenave et al. 2018). During 2005–16, increasing global ocean mass observed by the NASA Gravity Recovery and Climate Experiment (GRACE), 2.5 ± 0.4 mm yr^{-1}, contributed about two-thirds of the GMSL trend. The positive trend in ocean mass primarily resulted from melting of glaciers and ice sheets (Sections 2c, 5,6), but these contributions from land ice were partially offset by increased hydrological storage of fresh water on land, −0.7 ± 0.2 mm yr^{-1} (Reager et al. 2016). Unfortunately, failure of an accelerometer on board one of the GRACE satellites and degrading batteries resulted in only five months of valid GRACE observations during 2017 (January and March–June). The mission was finally terminated in October 2017 with no additional scientific observations. Although the GRACE-FO mission was launched in May 2018 and scientific data were collected, the processing centers are still evaluating and calibrating the data. Thus, ocean mass observations for 2018 are not available as of this writing. Steric (i.e., density-related) sea level rise (0–2000 m) observed by the Argo profiling float array during 2005–16, 1.1 ± 0.2 mm yr^{-1}, which is mostly due to ocean warming, accounts for most of the balance of GMSL change during the GRACE period. Steric sea level rise updated for 2005–18 increases to 1.3 ± 0.2 mm yr^{-1}.

Annual GMSL from altimetry observations increased by 0.4 cm from 2017 to 2018 (Fig. 3.15a). Annual global mean steric sea level observed by Argo did not appreciably change from 2017 to 2018 (Fig. 3.15a). The lack of steric change suggests that the increase in GMSL was almost entirely due to an increase in ocean mass, but as discussed above, observations of ocean mass were not possible during 2018. We can, however, infer the change in ocean mass by subtracting global mean steric sea level from GMSL (Fig. 3.15a) with the assumption that steric changes below 2000 m do not contribute significantly at interannual timescales. The inferred ocean mass curve is highly correlated with the observed mass curve during 2005–16, suggesting that the inferred ocean mass curve during 2017–18 represents a reasonable surrogate in the absence of mass observations.

Regional sea level change can differ substantially from the global mean. The total amount of GMSL change from 1993–2018 is less than 10 cm (Fig. 3.15a), but multiple regions around the global ocean have experienced 15–20 cm during the same period. During the altimetry era, east–west differences in sea level change across the Pacific—and specifically enhanced rise in the western tropical Pacific—resulted from fluctuations in trade winds, which strengthened during a multi-decadal trend toward the La-Niña-like phase of the PDO during the first 15–20 years of the satellite record (e.g., Merrifield 2011). Enhanced sea level rise has also occurred over 30°–60°S in the South Pacific and South Atlantic basins, which has been attributed in the Pacific to deep-ocean warming (Volkov et al. 2017). Finally, the Kuroshio Extension region stands out as an area of enhanced sea level rise due to both wind-forced and eddy-forced warming (Qiu et al. 2015).

Positive annual sea level anomalies spanned much of the global ocean during 2018 (Fig. 3.16a), which

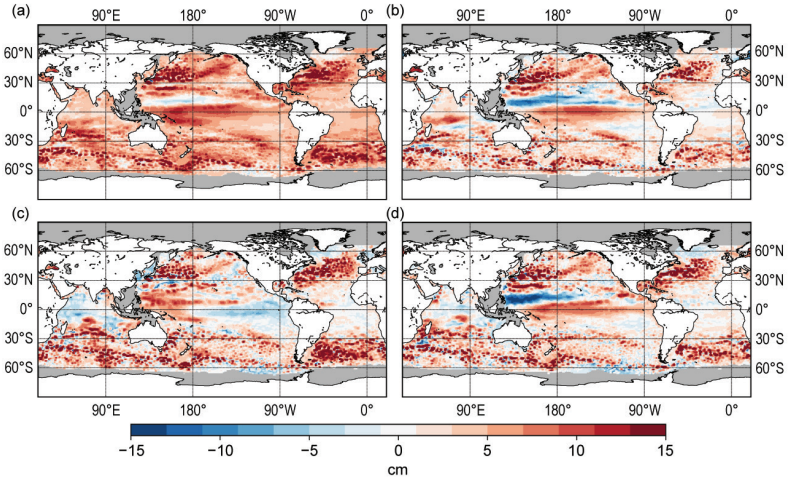

Fig. 3.16. (a) Annual average sea level anomaly during 2018 relative to the average sea level at each location during 1993–2018. (b) Average 2018 sea level anomaly minus 2017. (c) Average sea level anomaly during DJF of 2018 relative to the DJF average during 1993–2018. (d) Same as (c), but for SON. GMSL was subtracted from panels c–d to emphasize regional, non-secular change. Altimetry data was obtained from the gridded, multi-mission product maintained by the Copernicus Marine and Environment Monitoring Service (CMEMS).

is consistent with the global pattern of sea level rise since 1993 (Fig. 3.15b). A notable exception to the above-normal sea levels is in the tropical northwestern Pacific where a zonal band of below-normal sea levels occurred during most of 2018. In the tropical North Pacific, the annual mean sea level decreased from 2017 to 2018 (Fig. 3.16b) and reached the lowest levels near the end of the year (Figs. 3.16c,d). The area of sea level decrease extends from near the Philippines, eastward through most of Micronesia, and includes the area around Hawaii where the record high sea levels of 2017 (Yoon et al. 2018) returned to normal during 2018. Elsewhere in the Pacific, sea levels increased relative to 2017 nearly everywhere, except for small-scale decreases associated with upwelling mesoscale eddy activity such as around the Kuroshio Current region (Fig. 3.16b; e.g., Qiu et al. 2015). Increased sea levels in the equatorial Pacific are consistent with the warming ocean there resulting from the potential El Niño of 2018/19 (Section 4b). During 2018, the decrease in sea level in the tropical northwestern Pacific (the change from December–February to September–November exceeded –25 cm) and the increase of similar magnitude in the equatorial central Pacific (Fig. 3.16c,d) are consistent with the OHCAs (Fig. 3.4b), although the prolonged high sea levels in the tropical southwestern Pacific (e.g., around the Samoan Islands) are unusual compared to previous El Niño development.

In the Atlantic Ocean, sea level tendencies from 2017 to 2018 were positive in the tropical northwestern basin (generally +5 cm to +10 cm), whereas smaller changes (typically ±5 cm) occurred near the eastern boundary, along the equator, and in the tropical South Atlantic (Fig. 3.16b). Notable changes during 2018 (Fig. 3.16c,d) were the rising sea levels around Florida, the Bahamas, and the Greater Antilles (~10 cm increase), consistent with locally higher surface heat flux (Fig. 3.11b) and ocean heat content (Fig. 3.4b). Wind-stress anomalies in the tropical North Atlantic were also conducive for generation of downwelling Rossby waves (i.e., negative Ekman vertical velocity; Fig. 3.13d), which have been associated with past high sea level anomalies near Florida (Calafat et al. 2018). Poleward of 30°N/S, sea level mostly increased compared to 2017 (Fig. 3.16b), although there were small-scale decreases associated with upwelling eddies (Qiu et al. 2015). The change pattern in the higher latitudes (30°–60° N/S) is similar in the North and South Pacific as well as the South Indian Oceans, where some of the largest sea level increases during the satellite altimetry era have occurred (1993–2018, Fig. 3.15b).

In the North Indian Ocean, the greatest changes relative to 2017 were primarily related to eddy activity near the Arabian Peninsula and the east coast of India, although there was a basin-scale rise in sea level (Fig. 3.16b), which is consistent with the regional increase in surface heat flux (Fig. 3.11b) as well as downwelling Ekman vertical velocity (Fig. 3.13d). In the southern tropical latitudes, larger positive sea level anomalies during 2018 (+10 cm; Fig. 3.16a) are consistent with the above-normal surface heat flux in the region (up to +30 W m^{-2}; Fig. 3.11a). Even higher sea level anomalies poleward of 20°S (exceeding +15 cm east of Madagascar) are collocated with downwelling Ekman vertical velocities associated with regional wind-stress anomalies (Fig. 3.13).

Ongoing trends and year-to-year changes in sea level impact coastal communities by increasing the magnitude and frequency of positive sea level extremes that cause flooding and erosion. In many areas, coastal infrastructure is currently exposed to nuisance-level (i.e., minor-impact) flooding when water levels exceed a threshold defined by the top 1% of observed daily maxima from a global network of tide gauges (Sweet et al. 2014). These thresholds vary geographically (Fig. 3.17a) but are typically around 0.5 m above mean higher high water (MHHW)—the average of observed daily maxima—and are expected to be exceeded 3–4 times per year. Most locations along the U.S. East Coast experienced greater-than-expected numbers of exceedances during 2018 (Fig. 3.17b), which is a continuation of enhanced numbers of exceedances during 2017 (Fig. 3.17c) and is related to positive sea level trends (Fig. 3.15b) and 2018 anomalies (Fig. 3.16a) in the region. Year-over-year increases in threshold exceedances occurred on a majority of islands across the tropical South Pacific, while year-over-year decreases occurred on a majority of islands across the tropical North Pacific (Fig. 3.17c). These changes in the tropical Pacific directly relate to changes in mean sea level of the same signs in these regions from 2017 to 2018 (Fig. 3.16b). The increase in exceedances in the eastern Atlantic from 2017 to 2018 (Fig. 3.17c) represents a return to expected numbers of exceedances (Fig. 3.17b) after few exceedances occurred in the region during 2017.

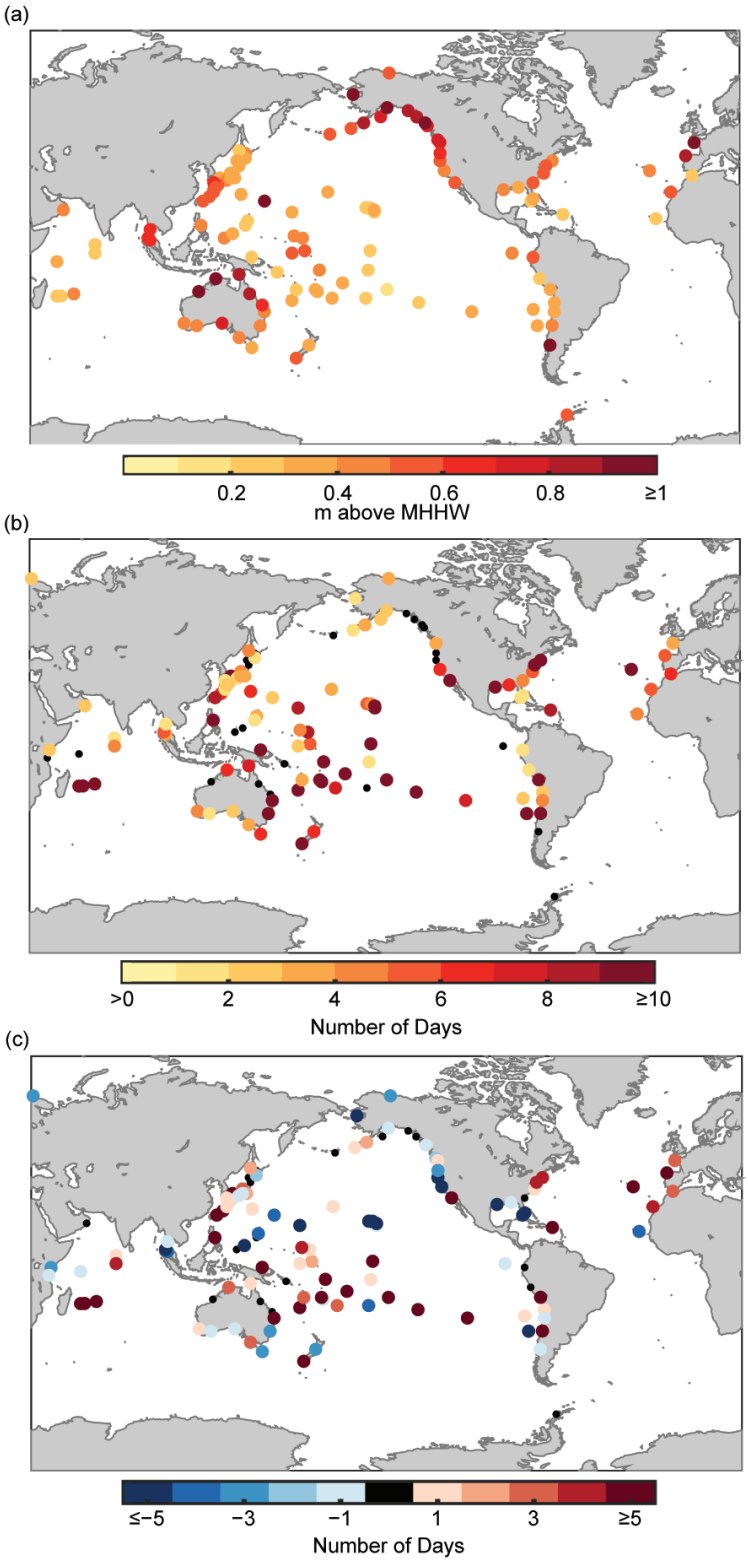

Fig. 3.17. (a) Nuisance-level flooding thresholds defined by the level of the top 1% of observed daily maxima during 1999–2017 from tide gauge records. Units are in meters above MHHW calculated over 1999–2017. (b) Number of daily maximum water levels during 2018 above the thresholds in (a). (c) Same as in (b), but for 2018 minus 2017. Small, black circles in (b) and (c) indicate a value of zero. Daily maximum water levels were calculated from hourly tide gauge observations obtained from the University of Hawaii Sea Level Center Fast Delivery database. Only records with at least 80% completeness during 1999–2017 and 80% completeness during 2018 were analyzed.

SIDEBAR 3.2: 2018 FLORIDA RED TIDE BLOOM—C. KELBLE, M. KARNAUSKAS, K. HUBBARD, G. GONI, AND C. STREETER

Red tides caused by the dinoflagellate, *Karenia brevis*, are a naturally occurring phenomenon in the Gulf of Mexico, including the west Florida shelf (Steidinger 2009). This alga blooms nearly annually in the coastal waters of southwest Florida and occurs less frequently along Florida's Panhandle and Atlantic coasts (Steidinger 2009). There are reports suggestive of red tides from early European explorers dating back to the early 1500s, but perhaps the earliest well-documented *K. brevis* bloom on the west Florida shelf was in 1844 (Magaña et al. 2003). Mortalities in marine animals and human respiratory irritation caused by toxins produced by *K. brevis* during red tide events can be widespread (Steidinger 2009). The duration, spatial extent, and movement of the red tide are factors that influence considerable variations in severity of impacts on the ecosystem and human communities. The 2017–19 bloom was the fifth longest-lasting bloom since 1953, when more intensive state monitoring was instituted. This 16-month event resulted in impacts on Florida's Panhandle, southwest, and east coasts including extensive wildlife mortalities and strandings, numerous reports of human respiratory irritation, persistent shellfish harvest area closures, and/or other undesired consequences including economic ones (Fig. SB3.2).

The 2017–19 red tide bloom impacted southwest Florida most severely, including known hotspots (i.e., the greater Charlotte Harbor and Tampa Bay areas). From late 2017 to early 2019, *K. brevis* cells persisted in these general areas (Fig. SB3.2). Not only was this an intense, long-lasting red tide in southwest Florida, it was also geographically widespread. After the passage of Tropical Storm Gordon in early September 2018, the bloom in southwest Florida intensified, and bloom concentrations (>100000 cells per liter) were first detected in Florida's Panhandle and endured through November. At the end of September and through October 2018, bloom concentrations were also detected on Florida's east coast. The northwest and east coast blooms were thus comparatively short-lived relative to the southwest bloom. It is worth noting that these occurrences took place in late summer into fall, when new bloom initiation most typically occurs in southwest Florida, and that northwest and southwest blooms are hypothesized to share a single offshore initiation zone; cells are transported from initiation zones toward shore by subsurface currents. Transport of cells from southwest Florida to the east coast of Florida has been previously documented (Weisberg et al. 2009) and can occur when cells are transported southward and then entrained in the Florida Current; sampling in October 2018 also revealed the presence of red tide in the Florida Keys and the currents during this time period support transport of the southwest bloom to the east coast (Fig. SB3.3).

Red tides have significant negative impacts on the ecosystem, including fisheries. The effects of red tide on marine organisms are both direct via brevetoxins or low dissolved oxygen and indirect via changes in the food web (DiLeone and

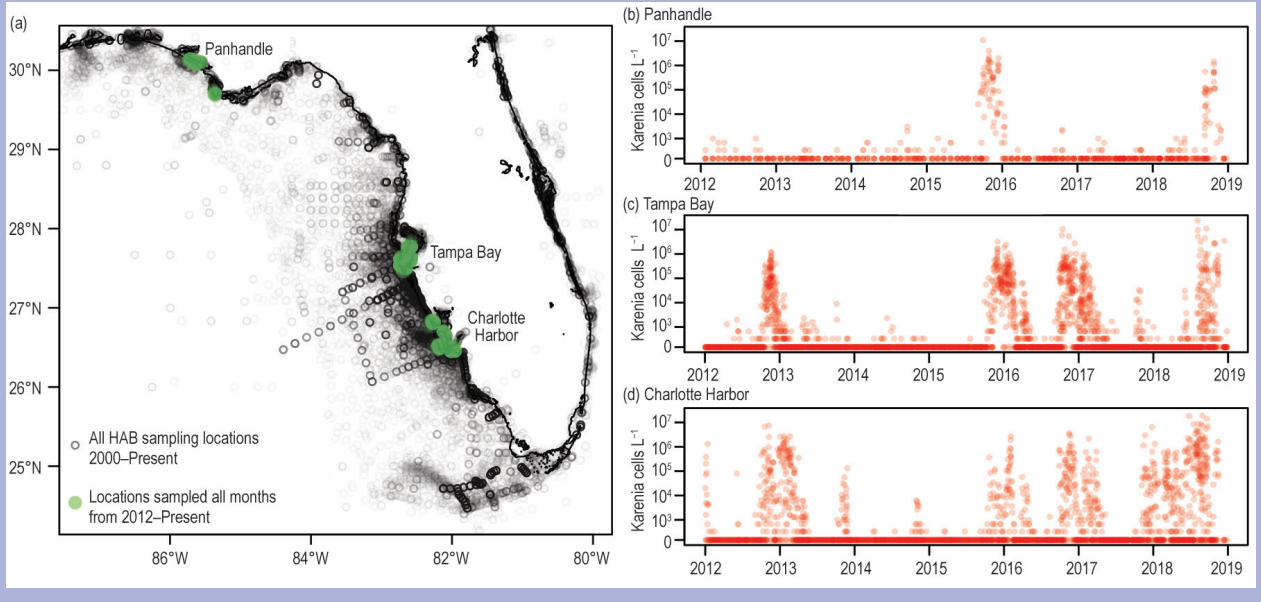

FIG. SB3.2. Left: All sampling locations for *Karenia brevis* cell counts throughout Florida from 2000 through the end of 2018. Right: *Karenia brevis* cell counts (cells/l) for locations, binned as 1/10° longitude and latitude cells, which have been sampled at least monthly since 2012.

Ainsworth 2019). The 2017–19 red tide on Florida's west coast coincided with substantial decreases in fisheries landings as evidenced by the landings for five common commercial categories in Lee and Charlotte counties, near Charlotte Harbor (Table SB3.1). All of the landings decreased substantially in 2017 and 2018, and reports from fishermen indicated that fishing was challenging with little success during the latter part of 2018. Based, at least in part, on these concerns, an emergency rule was requested by the Gulf of Mexico Fisheries Management Council to decrease the red grouper quota. In addition to fisheries impacts, an unusual mortality event affected 149 dolphins along with manatees and turtles beginning in July 2018. These observations collectively underscore the significance of events like this on local fisheries and help direct efforts to assess further ecological impacts related to this severe bloom in years to come.

Red tides cause significant economic losses to coastal communities in Florida not only through declines in fisheries landings, but also through negative impacts on tourism. These are two of the biggest industries in the state, and thus their losses propagate from locally impacted communities. The Fort Myers Florida Weekly surveyed 156 businesses in Fort Myers Beach. The businesses reported $48.8 million (U.S. dollars) in lost revenue during the 13-week period from July 27, 2018 through October 26, 2018 (https://fortmyers.floridaweekly.com/articles/in-the-wake-of-red-tide/). Although events such as the substantial 2017–19 red tide clearly have widespread detrimental effects, these events also provide opportunities to study related mechanisms, critical for furthering the ability to predict future blooms and considering potential mitigation strategies.

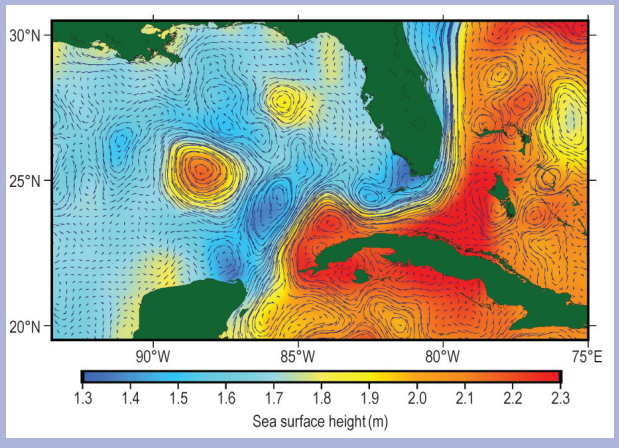

Fig. SB3.3. Satellite altimetry-derived sea surface height (background color) and surface currents (arrows) for 10 Oct 2018. The currents suggests southerly flow on the west Florida shelf that would allow for advection of red tide to the east coast of Florida.

Table SB3.1. Fisheries landings in thousands of pounds from Charlotte and Lee counties in Florida (trip ticket data from the Florida Fish and Wildlife Commission).

Species	2012	2013	2014	2015	2016	2017	2018
Red Grouper	254	220	386	342	429	352	197
Mullet	3111	3455	3401	2963	3082	1790	1401
Stone Crabs, Jumbo	29	21	11	29	27	9	5
Stone Crabs, Large	59	54	54	83	80	42	22
Stone Crabs, Medium	71	76	80	91	95	76	39

g. Surface currents—R. Lumpkin, G. Goni, and K. Dohan

This section describes ocean surface current changes, transports derived from ocean surface currents, and features such as rings inferred from surface currents. Surface currents are obtained from in situ (global array of drogued drifters and moorings) and satellite (altimetry and wind stress) observations. Transports are derived from a combination of sea surface height anomaly (from altimetry) and climatological hydrography. See *State of the Climate in 2011* for details of these calculations. Zonal surface current anomalies are calculated with respect to 1993–2007 climatology and are discussed below for individual ocean basins.

1) Pacific Ocean

In 2018, the Pacific basin exhibited an annual mean zonal eastward current anomaly of 10–15 cm s^{-1} from 130°E–135°W, with peak anomalies shifting from 6°N at the western edge to 8°N at the eastern edge (Fig. 3.18a). This anomaly band indicates that there was a strengthened North Equatorial

Countercurrent (NECC) extending farther north than in climatology. Because 2017 was characterized by westward anomalies in this latitude band with peak values in the central basin (125°–145°W), the 2018–minus–2017 map (Fig. 3.18b) has larger eastward anomalies here. This shift in the NECC was likely associated with the co-located wind stress anomalies seen in 2018 (Fig. 3.13a), which veered from westerly in the western Pacific to south-southwesterly in the central Pacific.

Figure 3.19 shows the development of zonal geostrophic current anomalies with respect to monthly climatology, averaged season by season. In December–February 2017/18 (Fig. 3.19a), the largest anomalies were 25–30 cm s^{-1} eastward between the equator and 2°S, 115°–170°W, where the seasonal mean current is near zero. This countercurrent, associated with a seasonally shoaling equatorial undercurrent, does not develop until April–May in climatology derived from drifters drogued at 15-m depth (www.aoml.noaa.gov/phod/gdp/mean_velocity.php). Along these same longitudes, a band of positive (eastward) anomalies at 8°–10°N and negative (westward) anomalies at 3°–5°N indicated that the NECC was strengthened and shifted anomalously north of its climatological position, while the northern core of the South Equatorial Current (nSEC) was strengthened at 3°–4°N. The eastward anomalies intensified March–May (Fig. 3.19b), indicating that the NECC was 30 cm s^{-1} faster than its climatological strength of ~35 cm s^{-1}, and the countercurrent at 0°–2°S, where climatological currents are near zero, was 25 cm s^{-1}. Westward anomalies centered on the nSEC diminished, however. During June–August (Fig. 3.19c), anomalies not associated with the NECC weakened significantly and, apart from that current system, the basin-scale zonal currents were close to climatology. Large eastward anomalies of 30–35 cm s^{-1} persisted in the western NECC at 160°E–130°W, centered near the climatological core latitude of the NECC at 7°–8°N. The anomalies in the NECC weakened significantly (to 15–20 cm s^{-1}) during September–November (Fig. 3.19d), while eastward anomalies of 25–30 cm s^{-1} developed along the equator in the eastern basin at 100°–150°W.

Shifts in the location of the Kuroshio Jet are associated with a decadal stable/unstable oscillation (Qiu and Chen 2005). The Kuroshio shifts to the north when it intensifies and becomes stable thus lowering eddy kinetic energy (EKE). Averaged in the downstream Kuroshio Jet region 141°–153°E, 32°–38°N (Qiu and Chen 2005), EKE was low in 1994/95, elevated in 1999–2001, low in 2002/04, high in 2005–08, and then decreased from 2009 to 2018. Since 2015, EKE has remained relatively steady (at annual to interannual time scales) and lower than the 1993–2018 average in the downstream Kuroshio Jet region, indicating that the system is in its stable mode, while exhibiting intra-annual variations such as a short-lived increase in EKE in mid-2016. During 2018, EKE in the region averaged 0.102 $m^2 s^{-2}$ compared to the 1993–2017 average of 0.117 $m^2 s^{-2}$, while maximum speeds were at 35.6°N, slightly north of the climatological average latitude of 35.3°N.

The equatorial Pacific current system advects waters across the basin, contributing to anomalies in the SST fields. Historically, surface current (SC) anomalies in this region are a strong indicator of upcoming SST anomalies with SC anomalies leading SST by several months and a reversal of the SC anomaly usually coinciding with peak SST anomaly. This behavior can be seen in the first principal EOFs of SC anomaly and SST anomaly across the tropical Pacific basin (Fig. 3.20). The maximum lagged correlation between SC and SST is R = 0.65 for 1993–2018, with SC leading SST by 76 days. The year 2018 began with negative SST anomalies, with a maximum negative SST EOF amplitude of −1.2σ in early January, rising for most of 2018, and peaking in November

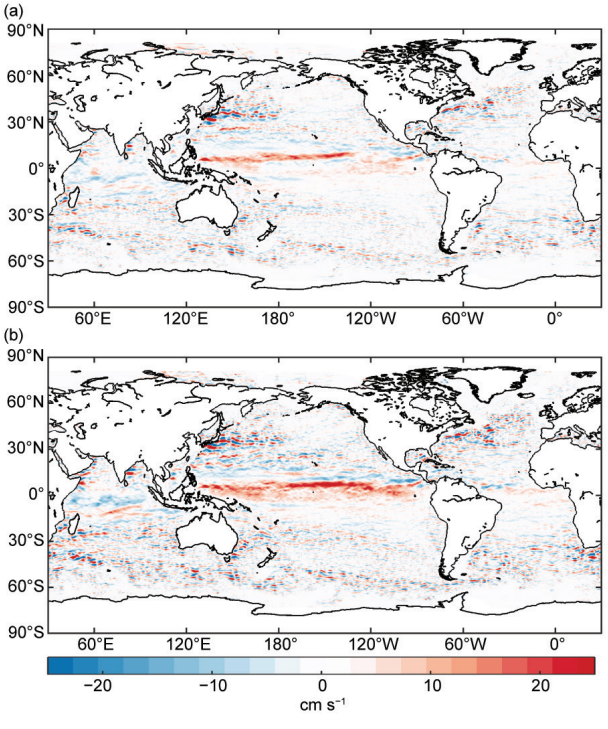

Fig. 3.18. Annually-averaged geostrophic zonal current anomalies (cm s^{-1}) for (a) 2018 and (b) 2018–minus–2017 derived from a synthesis of drifters, altimetry, and winds. Positive (red) is eastward; negative (blue) is westward.

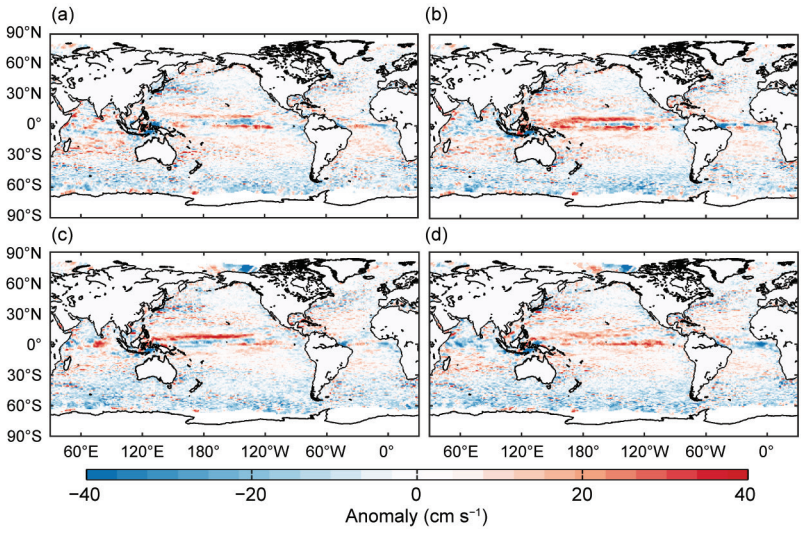

Fig. 3.19. Seasonally-averaged zonal geostrophic anomalies with respect to seasonal climatology, for (a) Dec 2017–Feb 2018, (b) Mar–May 2018, (c) Jun–Aug 2018, and (d) Sep–Nov 2018.

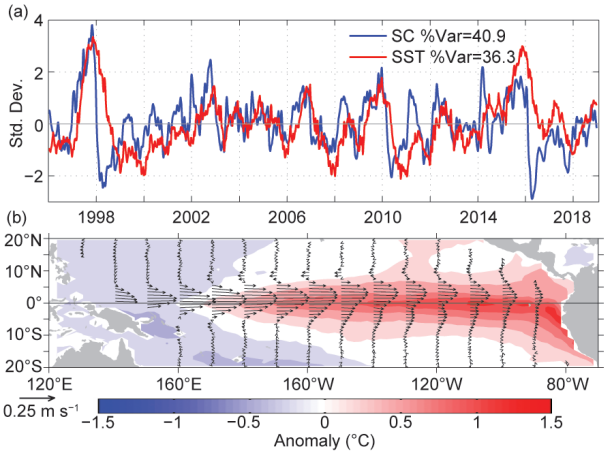

Fig. 3.20. Principal EOFs of surface current (SC) and of SST anomaly variations in the Tropical Pacific from the OSCAR model (Bonjean and Lagerloef, 2002). Top: amplitude time series of the EOFs normalized by their respective standard deviations. Bottom: spatial structures of the EOFs.

at 0.9. The SC anomalies rose from their minimum of –1.8 in October 2017, consistent with the lagged rising SST anomalies, then experienced negative anomalies from May to September, down to –0.9 in mid-July, before rising to positive values for the rest of 2018, with a maximum of 0.7 in October. The year was unusual in that while SST anomalies did experience some slowing in their rising in July–September, it was not nearly as significant as the reversal in SC. The year ended with a reversal of SC anomalies and a decrease in positive SST anomalies.

2) Indian Ocean

At basin scales, 2018 annually-averaged zonal currents in the Indian Ocean basin were very close to climatology, with large-scale anomalies weaker than ±5 cm s^{-1} (Fig. 3.18a). In contrast, 2017 was characterized by equatorial eastward anomalies of ~8 cm s^{-1} and westward anomalies of ~15 cm s^{-1} at 10°S in the eastern half of the basin; thus, the 2018–2017 map (Fig. 3.18b) reflects these 2017 anomalies with reversed sign.

The season-by-season maps of zonal current anomalies (Fig. 3.19) show that strong anomalies were only present in June–August 2018, when >20 cm s^{-1} eastward anomalies were present at 3°S–2°N, 70°–85°E. These anomalies are consistent with a strengthened southwest monsoon current extending farther north than in the seasonal climatology. In these months in this longitude band, the climatological southwest monsoon current has maximum speeds of 20–25 cm s^{-1} at 1°–2°S, while in 2018 the maximum speeds were 40–50 cm s^{-1} at 1°N–3°S.

3) Atlantic Ocean

Annual mean zonal currents in the tropical Atlantic Ocean were close to their climatological values in 2018 (Fig. 3.18a). During December–February 2017/18 (Fig. 3.19a), a countercurrent of 20–25 cm s^{-1} was centered on 1°S in the longitude band 15°–40°W, where the climatological current is not significantly different from zero. This countercurrent was no longer present in March–May (Fig. 3.19b), while westward anomalies of –20 cm s^{-1} at 0.5°–1.5°N were associated with a strengthened nSEC. Tropical Atlantic currents were very close to climatology in June–August (Fig. 3.19c). In September–November, westward near-equatorial anomalies of –10 cm s^{-1} were present in the northern Gulf of Guinea.

The changes in transport and location of several key surface currents and associated mesoscale rings in the Atlantic Ocean basin are continuously monitored using satellite altimetry observations (www.aoml.noaa.gov/phod/altimetry/cvar/index.php). We present here the state of four key dynamic features in the Atlantic Ocean: (1) During 2018, satellite altimetry observations show that the number of rings shed by the Agulhas Current remained similar to the mean 1993–2018. The transport by these rings is indica-

tive of water mass properties exchanges between the Indian and Atlantic Oceans. (2) In the southwest Atlantic Ocean, the separation of the Brazil Current from the continental shelf break (located at 37.6°S in the mean) reveals the intrusion of subtropical waters into the subpolar region. Since 1993, this current has separated farther to the south from the continental shelf break by 3° latitude (c.f., Lumpkin and Garzoli, 2010; Goni et al., 2011). During 2017 the location of separation moved to the south by about 2° latitude (see www.aoml.noaa.gov/phod/altimetry/cvar/mal/BM_ts.php), the largest southward shift in the altimeter time period 1993–present. During 2018, this location remained unchanged. (3) To the north, the North Brazil Current, which transports waters from the South Atlantic into the North Atlantic basin, showed a slight increase in the number and size of the rings shed and in the number of rings that eventually made their way into the Caribbean Sea. This increased transport is important because the rings carry fresh Amazon River water into the Caribbean Sea, creating barrier layers that often contribute to Atlantic hurricane intensification. (4) Altimetry and cable measurements of the Florida Current during 2018 do not show any deviation from their expected annual mean values at 27°N.

h. Global ocean phytoplankton—B. A. Franz, I. Cetinić, E. M. Karaköylü, D. A. Siegel, and T. K. Westberry

Marine phytoplankton contribute roughly half the net primary production (NPP) on Earth, fixing atmospheric CO_2 into food that fuels global ocean ecosystems and drives biogeochemical cycles (e.g., Falkowski et al. 1998; Field et al. 1998). Phytoplankton growth is dependent on availability of light and nutrients (e.g., iron, nitrogen, phosphorous) in the upper ocean euphotic zone, which in turn is influenced by physical factors such as ocean temperature (e.g., Behrenfeld et al. 2006). SeaWiFS (McClain 2009) and MODIS (Esaias et al. 1998) are satellite ocean color sensors that provide observations of sufficient frequency and geographic coverage to globally monitor changes in the near-surface concentration of the phytoplankton pigment chlorophyll-*a* (Chl*a*; mg m^{-3}), and phytoplankton carbon biomass (C_{phy}; mg m^{-3}). While both quantities vary with phytoplankton abundance and thus serve as proxies for phytoplankton biomass, cellular Chl*a* can also vary significantly due to physiological response to light and nutrient conditions or changes in species composition (Diersen 2010; Geider et al. 1997). In combination, these two satellite products provide insight into multiple dimensions of environmental and climate-driven variability in phytoplankton biomass, composition, and physiology (Behrenfeld et al. 2008; Siegel et al. 2013; Westberry et al. 2016).

Here, global Chl*a* and C_{phy} distributions for 2018 are evaluated within the context of the continuous 21-year record provided through the combined observations of SeaWiFS (1997–2010) and MODIS on Aqua (MODISA, 2002–present). The NASA standard MODISA daytime SST product, version R2014.0, is used to provide context on the physical state of the oceans. All ocean color data used in this analysis correspond to NASA processing version R2018.0, which utilizes common algorithms and calibration methods to maximize consistency in the multi-mission satellite record. The R2018.0 Chl*a* product was derived using the algorithm of Hu et al. (2012), while Cphy was derived from the R2018.0 particle backscattering coefficient, b_{bp}, at 443 nm (Werdell et al. 2013) and a linear relationship between b_{bp} and C_{phy} as described in Graff et al. (2015). In combining the ocean color records, the overlapping period from 2003 through 2008 was used to assess and correct for residual bias between the two mission datasets.

To evaluate changes in the distribution of phytoplankton during 2018, mean values for MODISA Chl*a* and C_{phy} in each month of the year were subtracted from monthly climatological means for MODISA (2003–11). These monthly fields were then averaged to produce the global Chl*a* and C_{phy} anomaly maps for 2018 (Figs. 3.21a,b). Similar calculations were performed on MODISA SST (°C) data to produce an equivalent SST annual mean anomaly (Fig. 3.21c). The permanently stratified ocean (PSO) is defined as the region covering the tropical and subtropical oceans where annual average SST is greater than 15°C and is characterized by surface mixed layers that are typically low in nutrients and shallower than the nutricline (black lines near 40°N and 40°S in Fig. 3.21; Behrenfeld et al. 2006).

For 2018, Chl*a* concentrations (Fig. 3.21a) were suppressed 10%–30% relative to the climatological mean in the western warm pool and northern and southern regions of the tropical Pacific, as well as the western North Pacific and the western subtropical North Atlantic. These locations correspond to regions of strongly elevated SSTs (Fig. 3.21c). C_{phy} concentrations within the tropical Pacific show similar but weaker patterns of negative anomalies in the east (–5%) but neutral to positive anomalies (+5%) in the west, with C_{phy} anomalies generally more homogeneous across the Atlantic and Pacific Oceans (Fig 3.21b). Positive SST anomalies in these permanently stratified ocean regions generally coincide with shal-

lower surface mixed layer depths (MLD), exposing phytoplankton to prolonged daily sunlight exposures. Phytoplankton respond to this increased light by decreasing their cellular chlorophyll levels (Behrenfeld et al. 2015). Shallower MLDs might also indicate a decrease in vertical nutrient transport, adding to the physiological response of the cell and potentially driving additional decoupling of Chl*a* and C_{phy} anomalies due to decreased cellular chlorophyll to carbon ratios (Westberry et al. 2016). Coherent patches of elevated phytoplankton biomass, as evident from both Chl*a* and C_{phy} anomalies, were visible in the Arabian Sea and Bay of Bengal, the southern Pacific subtropical gyre, and the eastern equatorial and subtropical Atlantic. Outside of the PSO, a much weaker correlation was observed between phytoplankton biomass anomalies and SST anomalies, consistent with past reports (e.g., Franz et al. 2018). Notably, strong negative anomalies in SST were visible across the subpolar North Atlantic and the Labrador Sea (~1°C), but the biological response differed for these regions, as Chl*a* and C_{phy} demonstrated positive anomalies (+35% and +15% respectively) in the Labrador Sea, while both measurements were depressed (–15%) in the North Atlantic.

Seasonal changes in phytoplankton biomass in the permanently stratified ocean typically display two pronounced peaks, reflecting vernal increases in biomass in the Northern and Southern Hemispheres (Figs. 3.22a,b). Peaks in monthly climatological Cp_{hy} tend to trail behind peaks in Chl*a* with a 2-month delay, likely due to a reduction in phytoplankton chlorophyll to carbon ratios as the seasonal bloom progresses (e.g., Westberry et al. 2016). During 2018, however, primary and secondary peaks in Chl*a* (red circles in Fig. 3.22) occurred slightly earlier than the climatological norm, leading to some significant deviations that include anomalously high values in January and May–June and low values in September and October. During 2018, C_{phy} values generally remained within the interquartile range of monthly climatological distributions, except during October–November, when mean phytoplankton biomass peaked earlier than the climatology.

Over the 21-year time series of spatially integrated monthly mean Chl*a* within the PSO (Fig. 3.23a), concentrations varied by ~15% (±0.02 mg m^{-3}) around a long-term average of 0.142 mg m^{-3} (Fig. 3.23a). This variability includes significant seasonal cycles in Chl*a* distributions and responses to climatic events, as has been observed previously (e.g., Behrenfeld et al. 2006; Franz et al. 2018). C_{phy} over the same 21-yr period varied by ~5% (±1.25 mg m^{-3}) around an average of 23.7 mg m^{-3} (Fig. 3.23c).

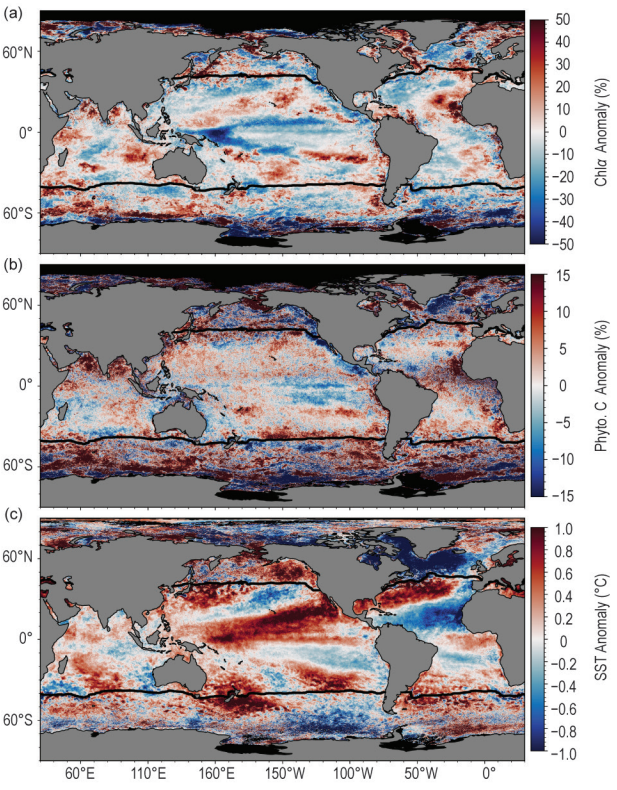

Fig. 3.21. Annual mean for 2018 of monthly (a) MODISA Chl*a*, (b) MODISA C_{phy}, and (c) MODISA SST anomalies, where monthly differences were derived relative to a MODISA 9-year climatological record (2003–11). Chl*a* and C_{phy} are stated as % difference from climatology, while SST is shown as an absolute difference. In each panel, black lines indicate the location of the mean 15°C SST isotherm delineating the PSO region.

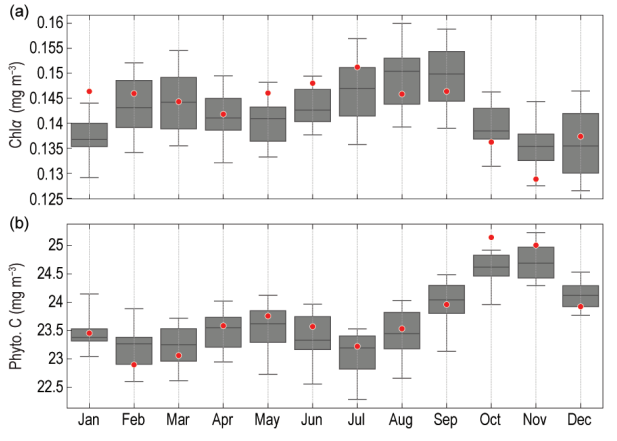

Fig. 3.22. Distribution of 2018 monthly means (red circles) for (a) MODISA Chl*a* and (b) MODISA C_{phy} for the PSO region, superimposed on the climatological values as derived from the combined time-series of SeaWIFS and MODISA over the 20-year period 1998–2017. The gray boxes show the interquartile range of the climatology, with black line for the median value and whiskers extending to the 5th and 95th percentiles.

Seasonal cycles in C_{phy} are more clearly delineated than those of Chl*a*, consistent with the assertion that C_{phy} represents true variability in phytoplankton biomass.

Chl*a* monthly anomalies within the PSO (Fig. 3.23b) show variations of ±10% (± 0.015 mg m^{-3}) over the multi-mission time series, with largest deviations generally associated with El Niño/La Niña events. This link between ENSO variability and mean Chl*a* response in the PSO is demonstrated by the correspondence of anomaly trends with the Multivariate ENSO Index (MEI; Wolter and Timlin (1998); presented in the inverse to illustrate the correlation, with R = −0.44). For 2018, Chl*a* anomalies were relatively small (±3%), consistent with weak ENSO conditions. Similar comments can be made about the C_{phy} anomaly trends, which show nominal to slightly elevated values in 2018 and also track well with the MEI over the 21-year timeseries (R = −0.39).

Variability and trends in Chl*a* reflect both adjustments in phytoplankton biomass and physiology (or health), while C_{phy} reflects changes in biomass alone. Both of these properties are mechanistically linked to physical conditions of the upper ocean, as well as to ecological interactions between phytoplankton and their zooplankton predators. Unraveling the diversity and covariation of factors that influence Chl*a* concentrations is essential for correctly interpreting the implications of Chl*a* anomalies on ocean biogeochemistry and food webs. For example, inverse relationships between Chl*a* and SST can emerge from changes in either mixed-layer light levels or vertical nutrient flux, but these two mechanisms have opposite implications on phytoplankton NPP (Behrenfeld et al. 2015). An additional complication is that measured changes in ocean color often contain a contribution from colored dissolved organic matter (Siegel et al. 2005) or from the changing phytoplankton population, with its type-specific optical characteristics (Dierssen 2010) that can be mistakenly attributed to changes in Chl*a* (Siegel et al. 2013). C_{phy} provides a more direct measurement of phytoplankton biomass that is insensitive to changes in physiological status of the cell, and thus offers complementary information on the state of the oceans. Future satellite missions, such as the planned hyperspectral Plankton, Aerosol, Cloud, ocean Ecosystem mission (PACE), will enable the rigorous separation of phytoplankton absorption features from non-algal features, as well as the assessment of changes in phytoplankton species or functional group distributions (Werdell et al. 2019). Such data will provide a major step forward in our ability to disentangle the impacts of climate forcing on global phytoplankton communities.

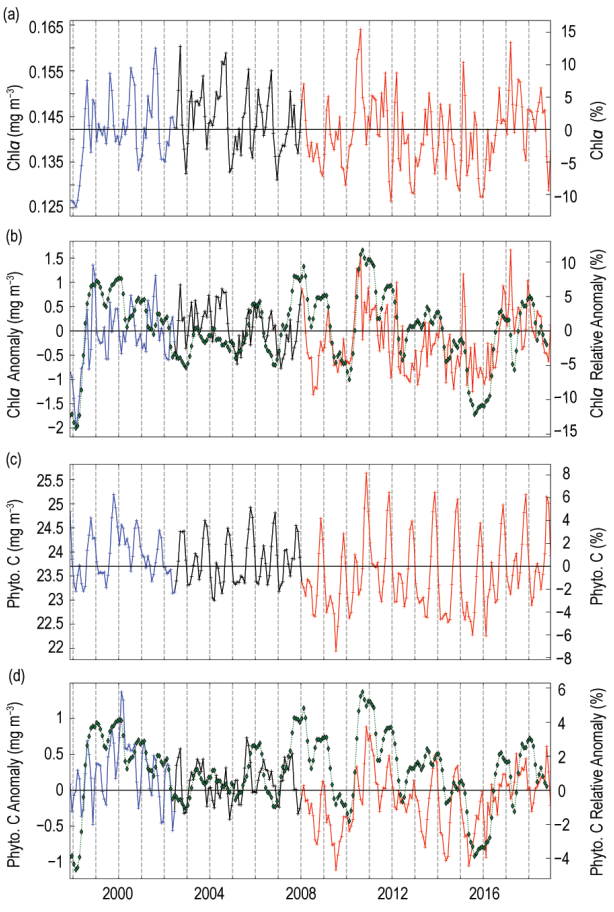

Fig. 3.23. 21-year, multi-mission record of Chl*a* and C_{phy} averaged over the PSO for SeaWiFS (blue), MODISA (red), and combined (black). Panel (a) shows Chl*a* from each mission, with horizontal line indicating the multi-mission mean Chl*a* concentration for the region. Panel (b) shows the monthly Chl*a* anomaly from SeaWiFS and MODISA after subtraction of the 20-year multi-mission climatological mean (Fig. 3.22). Panel (c) and (d) show the same as (a) and (b) respectively, but for C_{phy}. Green diamonds show the MEI, inverted and scaled to match the range of the Chl*a* and C_{phy} anomalies.

i. Global ocean carbon cycle—R. A. Feely, R. Wanninkhof, B. R. Carter, P. Landschützer, A. J. Sutton, C. Cosca, and J. A. Triñanes

The global oceans play a major role in the global carbon cycle by taking up a significant fraction of the excess CO_2 humans release into the atmosphere every year. As a consequence of humankind's collective release of CO_2 emissions into the atmosphere from fossil fuel burning, cement production, and land use changes over the last two-and-a-half centuries, commonly referred to as "Anthropogenic CO_2 (C_{anth})," the atmospheric CO_2 concentration has risen from pre-industrial levels of about 278 ppm (parts per million) to about 408 ppm in 2018. The

atmospheric concentration of CO_2 is now higher than has been observed on Earth for at least the last 800 000 years (IPCC 2013). As discussed in previous *State of the Climate* reports, the global ocean is a major long-term sink for C_{anth}, which is the major cause of ocean acidification. Here the discussion is updated to include recent estimates of that sink. Over the last decade, the global ocean has continued to take up a substantial fraction of the C_{anth} emissions and therefore is a major mediator of global climate change. Of the 10.8 (±0.9) Pg C yr^{-1} C_{anth} released during the period 2008–17, about 2.4 (±0.5) Pg C yr^{-1} (22%) accumulated in the ocean, 3.2 (±0.8) Pg C yr^{-1} (29%) accumulated on land, and 4.7 (±0.1) Pg C yr^{-1} (44%) remained in the atmosphere with an imbalance of 0.5 Pg C yr^{-1} (Le Quéré et al. 2018). This decadal ocean carbon uptake estimate is a consensus view based on a combination of measured decadal inventory changes, models, and global air–sea CO_2 flux estimates based on surface ocean partial pressure of CO_2 (pCO_2) measurements from ships and moorings. Using ocean general circulation models that include biogeochemical parameterizations (OBGCMs) and inverse models that are validated with observations-based air–sea exchange fluxes and basin-scale ocean inventories, Le Quéré et al. (2018) have demonstrated that the oceanic C_{anth} sink has grown from 1.0 (±0.5) Pg C yr^{-1} in the 1960s to 2.5 (±0.5) Pg C yr^{-1} in 2017. Air–sea CO_2 flux studies reported here and shown in Fig. 3.24 indicate a greater ocean uptake than provided in Le Quéré et al. (2018), due to an increased estimate of 0.78 Pg C yr^{-1} riverine contribution. This higher estimate in carbon from rivers is applied to the whole time series shown in Fig. 3.24.

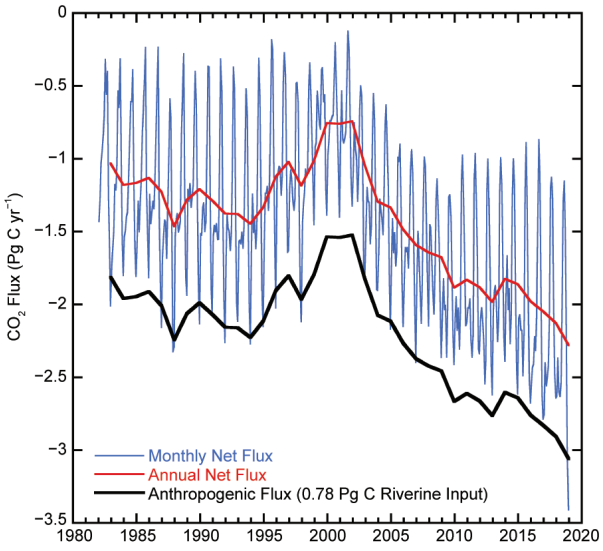

Fig. 3.24. Global annual (red line) and monthly (blue line) net CO_2 fluxes (Pg C yr^{-1}) for 1982–2018. The black line is the anthropogenic CO_2 flux, which is the net flux minus the riverine component of 0.78 Pg C yr^{-1}. Negative values indicate CO_2 uptake by the ocean.

1) Air–sea carbon dioxide fluxes

Ocean uptake of C_{anth} can be estimated from the net air–sea CO_2 flux derived from the bulk flux formula with air–sea differences in CO_2 partial pressure (ΔpCO_2) and gas transfer coefficients as input. A steady contribution of carbon from riverine runoff, originating from organic and inorganic detritus from land, revised upward from 0.45 to 0.78 Pg C yr^{-1} (Resplandy et al. 2018) is included to obtain the C_{anth} uptake by the ocean. The data sources for pCO_2 are annual updates of surface water pCO_2 observations from the Surface Ocean CO_2 Atlas (SOCAT) composed of mooring and ship-based observations (Bakker et al. 2016) and the Lamont-Doherty Earth Observatory (LDEO) database with ship-based observations (Takahashi et al. 2017). The increased observations and improved mapping techniques, including neural network methods and self-organizing maps (Landschützer et al. 2013, 2014; Rödenbeck et al. 2015), provide global pCO_2 fields on a 1° x 1° grid at monthly time scales annually. This allows investigation of variability on sub-annual to decadal time scales. The ΔpCO_2 and a parameterization of the gas transfer with wind described in Wanninkhof (2014) are used to calculate the air–sea CO_2 fluxes.

The monthly 2018 ΔpCO_2 maps are based on an observation-based neural network approach of Landschützer et al. (2013, 2014). The 2018 values are projections based on surface temperature, sea surface salinity, climatological mixed-layer depth, satellite chlorophyll-α, atmospheric CO_2, and the neural network for seawater pCO_2 developed from the data from the previous three decades. Changes in winds over time have a small effect on annual global air–sea CO_2 fluxes (Wanninkhof and Triñanes 2017). The C_{anth} fluxes from 1982 to 2018 suggest a decreasing ocean sink in the first part of the record and a strong increase from 2001 onward that continued into 2018 (Fig. 3.24). The amplitude of seasonal variability is large (≈ 1 Pg C) compared to the long-term trend with minimum uptake in the June–September timeframe. The C_{anth} air–sea flux of 3.1 Pg C yr^{-1} in 2018 is 36% above the revised 1996–2016 average of 2.24 (±0.4) Pg C yr^{-1}.

The average fluxes in 2018 (Fig. 3.25a) show the characteristic pattern of effluxes in the tropical regions and in the high-latitude Southern Ocean around 60°S, and uptake at mid-latitudes. The region with largest efflux is the equatorial Pacific. Coastal

upwelling regions including the Arabian Sea, off the coast of Mauritania, and the Peruvian upwelling system are significant CO_2 sources to the atmosphere as well. Large sinks are observed poleward of the subtropical fronts, and the frontal position determines the location of a maximum that is farther south and weaker in the Pacific sector of the Southern Ocean compared to the other basins.

In the Northern Hemisphere, there is a significant asymmetry in the sub-Arctic gyre with the North Atlantic being a large sink while the North Pacific is a significant source of CO_2. This is due in part to the position of the western boundary currents that are known CO_2 sinks at high latitudes. The Gulf Stream/North Atlantic drift extends farther north than the Kuroshio.

Ocean carbon uptake anomalies (Fig. 3.25b) in 2018 relative to the 1996–2016 average are attributed to the increasing ocean CO_2 uptake with time (Fig. 3.24) and to variations in large-scale climate modes. The long-term air–sea flux trend since 2000 is −0.7 Pg C decade^{-1} (or −0.16 mol m^2 yr^{-1} decade^{-1}), which leads to predominantly negative flux anomalies (greater ocean uptake). Despite this trend there are several large regions showing positive anomalies for 2018, notably the eastern equatorial Pacific, the subtropical North and South Pacific, and the high-latitude Southern Ocean. The increased effluxes in the eastern equatorial Pacific are related to a predominant negative sign of the Oceanic Niño Index (ONI) that followed an extensive period of predominantly positive ONI (El Niño) conditions in the preceding 20 years. This is borne out by the colder SST values (Fig. 3.26a) that indicate increased upwelling of waters with high CO_2 content. Positive anomalies in the Pacific subtropical regions (Fig. 3.25b) are related to the warm SST anomalies over the past year compared to the long-term average (Fig. 3.1a).

The differences between the air–sea CO_2 fluxes in 2018 compared to 2017 (Fig. 3.25c) are appreciable with anomalies roughly in the same regions as the difference of 2018 compared to the 20-year average. This indicates that conditions in 2018 are unique as compared to annual and decadal means. The increase in CO_2 effluxes in the eastern equatorial Pacific from 2017 to 2018 are associated with a return to more upwelling favorable conditions after the stalled El Niño in 2017. The Southern Ocean (south of 40°S) shows an increasing sink in the polar front region (≈ 50°S) and increasing source to the south for all three basins. The increasing sink near the polar front is partially compensated by a decreasing sink to the north. The correlations with SST anomaly (SSTA)

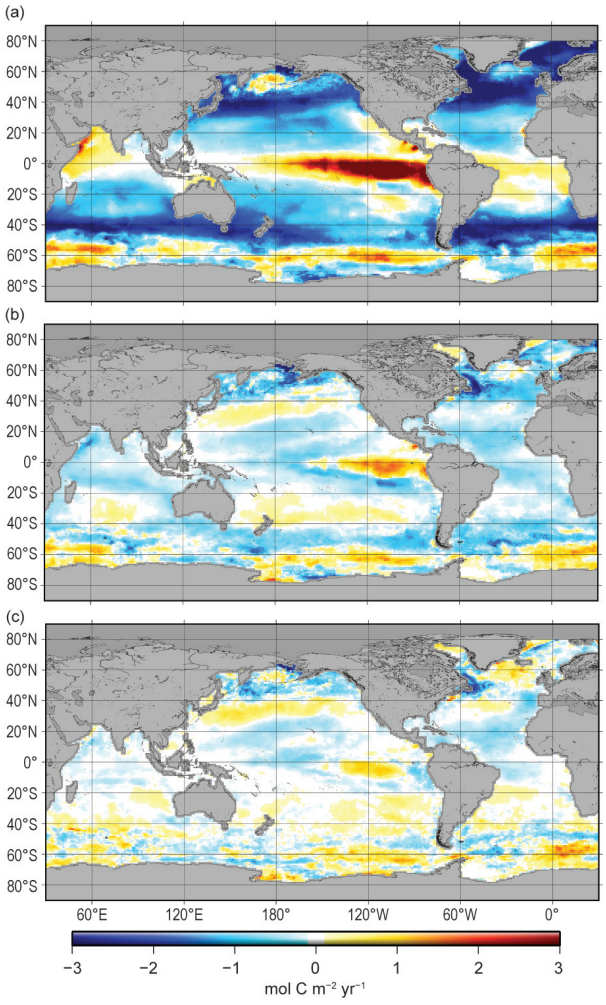

Fig. 3.25. Global map of (a) net air–sea CO_2 fluxes for 2018, (b) net air–sea CO_2 flux anomalies for 2018 relative to a 1996–2016 average, and (c) net air–sea CO_2 flux anomalies for 2018 minus 2017 values following the method of Landschützer et al. (2013), all in mol C m^{-2} yr^{-1}.

are more nuanced. The large negative SSTA in the eastern South Pacific centered at 60°S is attributed to deeper convection and upwelling contributing to the positive CO_2 flux anomaly (Fig. 3.25b). However, the large positive CO_2 flux anomaly in the eastern South Atlantic sector does not have a strong SSTA associated with it. The band of negative flux CO_2 anomalies compared to 2017 centered near 50°S is in a region with predominantly positive SSTA that suggests that in this band, SSTA and flux anomalies are decoupled. The North Pacific shows a large decrease in sink strength roughly following the path of the Kuroshio Current with a positive SSTA.

As detailed above, many of the pCO_2 and flux anomalies can be attributed to variations in large-scale climate modes and associated physical anomalies, notably temperature, but the causality is often

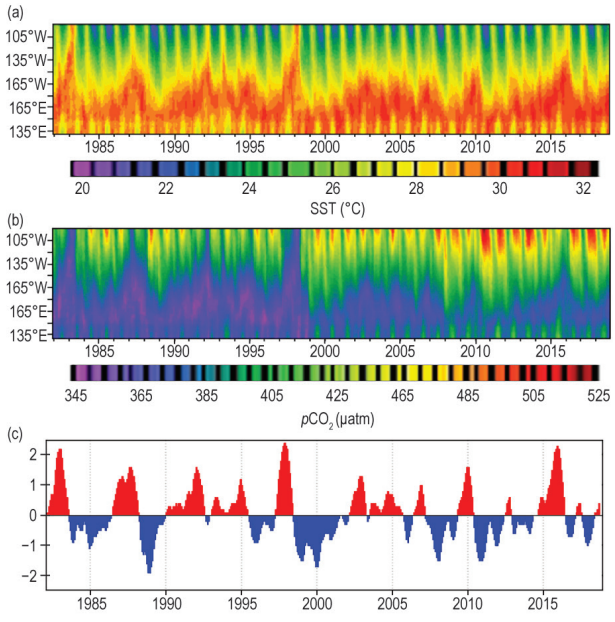

Fig. 3.26. Time-longitude plots of: (a) SST, (b) pCO_2, and the (c) ONI from 1982–2018 in the equatorial Pacific. Significant reductions in surface water pCO_2 values (low CO_2 outgassing) correspond with the El Niño events of 1982–83, 1986–87, 1991–94, 1997–98, 2002–05, 2006–07, 2009–10, and 2015–16. Significant enhancement of the pCO_2 values (high CO_2 outgassing) occurred with the strong La Niña events in 1984–85, 1998–99, 1995–96, 1998–2000, 2007–08, and 2011–12. 2018 was a normal non-El Niño year.

complex. For example, the behavior of pCO_2 with respect to temperature includes competing processes: thermodynamics dictate decreasing pCO_2 with decreasing SST, but waters originating from the deep with a cold temperature signal will have a high pCO_2. Moreover, the drawdown of pCO_2 due to biology is often associated with increasing temperature, but this depends on region and season.

The strong trend of increasing CO_2 uptake since 2002 has continued through 2018 with an increase of 0.15 Pg C above the 2017 estimate. This increase is well within the uncertainty of the estimate, but it is within the overall expectation that the ocean will remain an increasing sink as long as atmospheric CO_2 levels continue to rise. The sequestration of CO_2 by the ocean partially mitigates the atmospheric CO_2 rise, but it comes at a cost of increased acidification of surface and subsurface waters (Carter et al. 2017).

2) Interannual variability of pCO_2 in the tropical Pacific

From previous studies in the tropical Pacific, it is well-established that the oceanic variability of the air–sea exchange fluxes in this region are largely controlled by the surface ocean pCO_2 variability and wind forcing influenced by the nature and phasing of ENSO events (e.g., Feely et al. 1999, 2002, 2006; Ishii et al. 2009, 2014; Takahashi et al. 2009; Wanninkhof et al. 2013; Landschützer et al. 2014, 2016). The central and eastern equatorial Pacific is a major source of CO_2 to the atmosphere during non-El Niño and La Niña periods; it is near neutral during strong El Niño periods, and a weak source during weak El Niño periods. The warm El Niño phase of the ENSO cycle is characterized by a large-scale weakening of the trade winds, decrease in upwelling of CO_2 and nutrient-rich subsurface waters, and a corresponding warming of SST in the eastern and central equatorial Pacific. The opposite phase of the ENSO cycle, called La Niña, is characterized by strong trade winds, cold tropical SSTs, and enhanced upwelling along the equator. Figure 3.26 shows time-longitude plots of SST and pCO_2 for the region from 5°N to 10°S and 130°E to 95°W, and the Oceanic Niño Index (ONI) for the 36-yr period from 1982 through 2018. During the strong eastern Pacific El Niño events of 1982–83, 1997–98, and 2015–16, the cold waters of the eastern equatorial Pacific disappear and pCO_2 values are close to equilibrium with the atmosphere. However, during the weaker central Pacific El Niños of 1991–94, 2002–05, and 2006–07, the equatorial cold tongue is present but less pronounced, and pCO_2 values are higher than atmospheric values but lower than corresponding values for non-El Niño periods. The strongest El Niño event of 1997–98 had SST anomalies exceeding 4°C and the lowest pCO_2 values throughout most of the equatorial Pacific. In contrast, the 2015–16 El Niño event had SST anomalies that are similar to the 1997–98 event, yet the pCO_2 values were significantly higher because the upwelling-favorable winds were stronger in the easternmost and westernmost parts of the region. By 2018, the region returned to non-El Niño conditions and near-normal pCO_2 levels.

3) Long-term trends of surface ocean pCO_2

Another feature of the time series of pCO_2 measurements in the Pacific is the secular increase of oceanic pCO_2 in response to the rise in atmospheric CO_2. Studies from surface ships and moorings have demonstrated de-seasoned secular increases of surface ocean pCO_2 ranging from 2.3–3.3 µatm yr^{-1}; however, rates of change are lower during El Niño periods and higher during La Niña periods (Feely et al. 2006; Sutton et al. 2014). The highest rates of increase are observed in the eastern Pacific near 125°W. In the tropical Pacific, the strong influence of interannual and decadal variability on surface ocean pCO_2 makes it challenging to detect the anthropogenic change.

In the subtropical Pacific, time-series observations are long enough to detect the anthropogenic signal above the natural variability of the ocean carbon system (Sutton et al. 2017, 2019). De-seasoned monthly means of surface ocean pCO_2 observations at the Woods Hole Oceanographic Institution Hawaii Ocean Time-series Station (WHOTS) in the subtropical North Pacific and Stratus in the South Pacific gyre show anthropogenic trends of 1.8 ± 0.3 µatm yr^{-1} and 2.0 ± 0.3 µatm yr^{-1}, respectively (Fig. 3.27). These trends are not significantly different from each other or from the atmospheric (xCO_2) rate of increase at Mauna Loa Observatory of 2.2 ppm over this same time period.

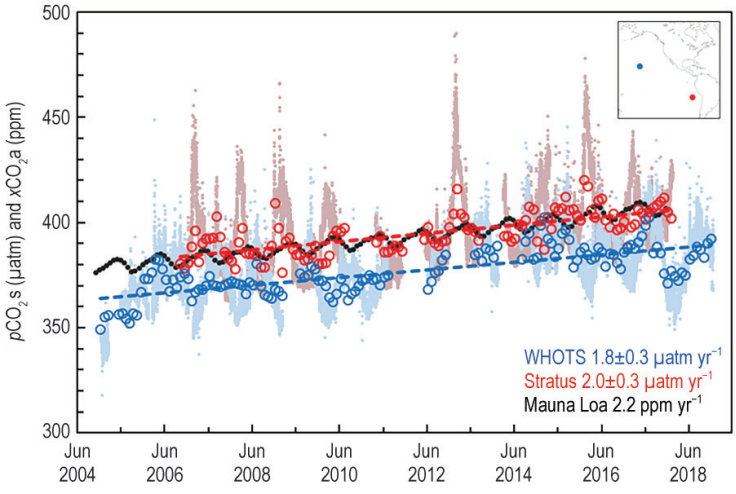

Fig. 3.27. Moored time-series observations of surface ocean seawater pCO_2 (pCO_2s) at the WHOTS (blue) and Stratus (red) sites in the subtropical Pacific (inset). Light colors are the high-resolution measurements and circles represent de-seasoned monthly means. Dashed lines represent trend of de-seasoned values. As a reference, the climate record of atmospheric CO_2 (xCO_2a) from Mauna Loa Observatory is shown in black (NOAA ESRL Global Monitoring Division, 2017).

4) Global ocean carbon inventories

Synoptic ship-based hydrographic measurements are the primary data with which the ocean carbon inventory, its anthropogenic component, and their changes are calculated. Ocean carbon inventories were first quantified in detail as part of the mid-1990s World Ocean Circulation Experiment (WOCE). The Climate Variability (CLIVAR) Repeat Hydrography Program in the mid-2000s and the Global Ocean Ship-based Hydrographic Investigations Program (GO-SHIP) since 2010 have re-measured a subset of the ocean-basin-spanning hydrographic cruise-tracks needed to update the inventories. Critically, these three programs each provided synoptic measurements of a range of seawater parameters with sufficient accuracy and spatial density (vertically and horizontally) in consistent locations to constrain anthropogenic carbon inventory changes with high confidence.

During the last year, a major analysis was completed quantifying the oceanic sink for CO_2 between 1994 and 2007 (Gruber et al. 2019). It was enabled by recent refinements to methods for processing interior ocean carbon data (e.g., Clement and Gruber 2018) and a data product released as the culmination of a decade of ship-based data synthesis and quality control work (Olsen et al. 2016). The analysis finds that ocean inventory increased by 34 (±4) PgC (i.e., 10^{15} g carbon) over this span at an average rate of 2.6 (±0.3) PgC $year^{-1}$. The scientists project this rate forward to estimate a global inventory for the year 2010 of 160 (±20) PgC. These findings are consistent with recent findings based on combinations of models and data (Khatiwala et al. 2013) and inversions of a variety of data types (DeVries et al. 2017). The rate of storage is increased relative to periods prior to 1994, but consistent with expectations from steadily increasing atmospheric CO_2 concentrations. However, broad regional variations were observed in the rate of CO_2 accumulation, suggesting that variability in ocean circulation and other modes of climate variability have important effects on ocean carbon concentrations on decadal timescales.

The patterns of accumulation vary by ocean basin (Fig. 3.28) in a manner consistent with broad-scale ocean circulation features, with significantly higher accumulation in shallower waters and in the warmer subtropical gyres, and less accumulation in the regions where dense waters upwell near the equator and in the subpolar oceans and the Southern Ocean. Higher accumulation occurs in shallower waters due to the close contact with the atmosphere, and slower accumulation occurs in upwelling waters that have been out of contact with the changing atmosphere for longer. As a secondary impact, higher accumulation occurs in warmer waters because elevating seawater chemistry drives reactions and gas exchange that result in the waters being more well-buffered against changing pCO_2, meaning atmospheric pCO_2 increases elevate the total carbon content of seawater by a larger amount before the seawater approaches air–sea equilibrium.

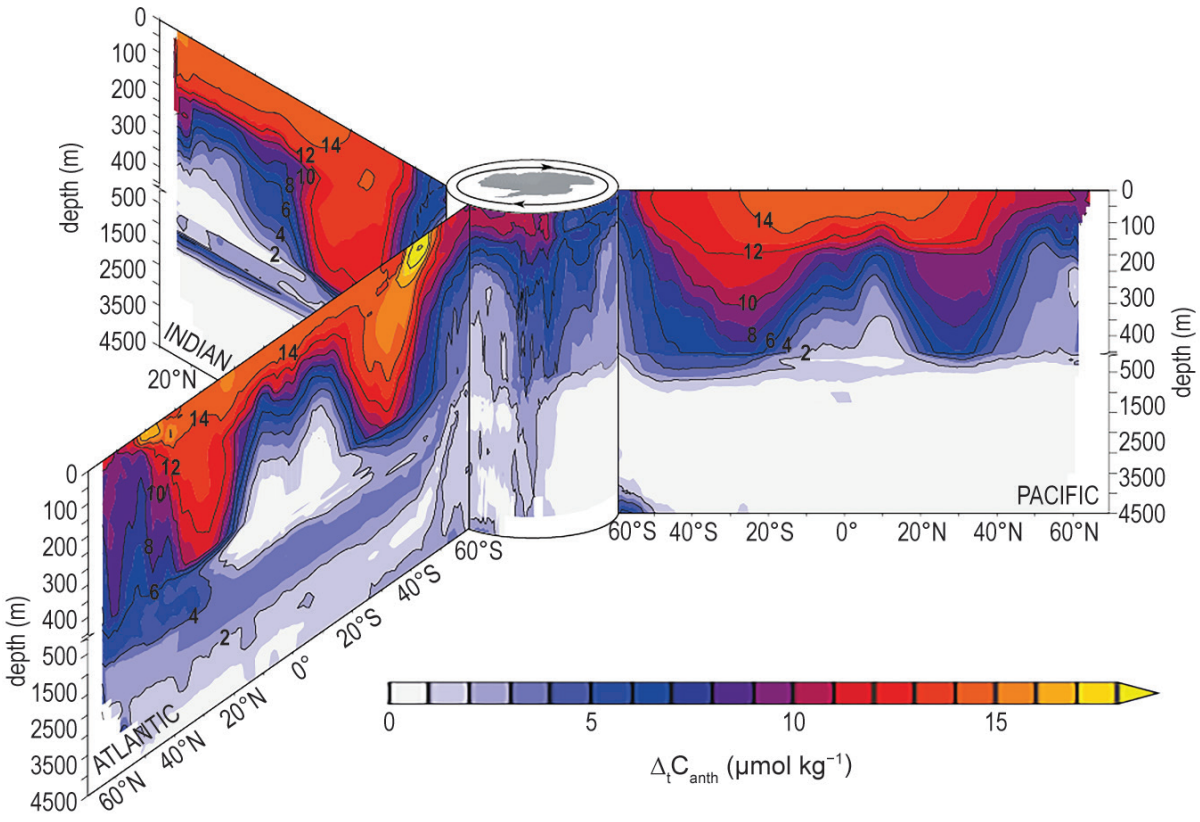

Fig. 3.28. Vertical sections of the accumulation of anthropogenic carbon in µmol kg^{-1} between the WOCE and CLIVAR periods of the repeat hydrographic records, as inferred by Gruber et al. (2019). Shown are the zonal mean sections in each ocean basin organized around the Southern Ocean (center). The upper 500 m are expanded and contour intervals are spaced at 2 µmol kg^{-1} of C_{anth}.